AFRL-AFOSR-JP-TR-2024-0038

Transonic Flutter of Hypersonic Skin-Panels

GAETANO CURRAO
NATIONAL CHENG KUNG UNIVERSITY
1, TA HSUEH RD.,
TAINAN CITY, , 70101
TWN

01/04/2024
Final Technical Report

DISTRIBUTION A: Distribution approved for public release.

Air Force Research Laboratory
Air Force Office of Scientific Research
Asian Office of Aerospace Research and Development
Unit 45002, APO AP 96338-5002

REPORT DOCUMENTATION PAGE

PLEASE DO NOT RETURN YOUR FORM TO THE ABOVE ORGANIZATION.

1. REPORT DATE	2. REPORT TYPE	3. DATES COVERED	
		START DATE	END DATE
20240104	Final	20210930	20230929

4. TITLE AND SUBTITLE
Transonic Flutter of Hypersonic Skin-Panels

5a. CONTRACT NUMBER	5b. GRANT NUMBER	5c. PROGRAM ELEMENT NUMBER
	FA2386-21-1-4118	
5d. PROJECT NUMBER	**5e. TASK NUMBER**	**5f. WORK UNIT NUMBER**

6. AUTHOR(S)
Gaetano Currao, Kung-Ming Chung, Wen-Lih Chen, Chih-Yung Wu, Zu Puayen Tan

7. PERFORMING ORGANIZATION NAME(S) AND ADDRESS(ES)
NATIONAL CHENG KUNG UNIVERSITY
1, TA HSUEH RD.,
TAINAN CITY 70101
TWN

8. PERFORMING ORGANIZATION REPORT NUMBER

9. SPONSORING/MONITORING AGENCY NAME(S) AND ADDRESS(ES)	10. SPONSOR/MONITOR'S ACRONYM(S)	11. SPONSOR/MONITOR'S REPORT NUMBER(S)
AOARD UNIT 45002 APO AP 96338-5002	AFRL/AFOSR IOA	AFRL-AFOSR-JP-TR-2024-0038

12. DISTRIBUTION/AVAILABILITY STATEMENT
A Distribution Unlimited: PB Public Release

13. SUPPLEMENTARY NOTES

14. ABSTRACT
This work is a numerical and experimental study of transonic panel flutter where alternative boundary conditions are explored. Hypersonic vehicles are subjected to strict low-weight requirements, thus skin-panel configurations are often optimized to maximize the payload. In the case of Skylon, a single-stage-to-orbit concept vehicle, one of these configurations involves the use of a series of discrete supports to stiffen thinner skin-panels, thus the question arises of whether this configuration offers improved stability margins also in the transonic regime. The geometrical boundary conditions are herein idealized as a rectangular panel clamped on all sides and with a rigid pin located in the middle. A numerical parametric analysis was conducted for a steel skin-panel for a range of altitude and Mach numbers to quantify the benefits of this panel configuration in the transonic, supersonic and low-hypersonic regime. A panel clamped on all sides and with a pin in the center was also tested in the transonic wind tunnel, where time-accurate displacement measurements were performed using laser sensors. The analysis of experiments and numerical simulations shows that transonic flutter is actually a forced response to an unsteady aerodynamic-load, rather than a two-way fluid-structure interaction. Higher natural modes, with a frequency close to the aerodynamic fluctuating pressure, are directly excited. Generally, the additional constraint in the center does not seem to add significant benefits in terms of dynamic stability in the transonic regime. Numerical results also suggest that the pin has a destabilizing effect at medium-low altitudes in the hypersonic regime. Conversely, flutter was successfully delayed in the supersonic regime.

15. SUBJECT TERMS

16. SECURITY CLASSIFICATION OF:			17. LIMITATION OF ABSTRACT	18. NUMBER OF PAGES
a. REPORT	b. ABSTRACT	c. THIS PAGE		
U	U	U	SAR	35

19a. NAME OF RESPONSIBLE PERSON	19b. PHONE NUMBER *(Include area code)*
JEFFREY NEWCAMP	315-227-7002

Standard Form 298 (Rev.5/2020)
Prescribed by ANSI Std. Z39.18

DISTRIBUTION A: Distribution approved for public release.

TRANSONIC FLUTTER OF HYPERSONIC SKIN-PANELS
AFOSR PROJECT : FA2386-21-1-4118
FINAL REPORT

Gaetano M.D. CURRAO
National Cheng-Kung University, Tainan City 701, Taiwan R.O.C.

This work is a numerical and experimental study of transonic panel flutter where alternative boundary conditions are explored. Hypersonic vehicles are subjected to strict low-weight requirements, thus skin-panel configurations are often optimized to maximize the payload. In the case of Skylon, a single-stage-to-orbit concept vehicle, one of these configurations involves the use of a series of discrete supports to stiffen thinner skin-panels, thus the question arises of whether this configuration offers improved stability margins also in the transonic regime. The geometrical boundary conditions are herein idealized as a rectangular panel clamped on all sides and with a rigid pin located in the middle. A numerical parametric analysis was conducted for a steel skin-panel for a range of altitude and Mach numbers to quantify the benefits of this panel configuration in the transonic, supersonic and low-hypersonic regime. A panel clamped on all sides and with a pin in the center was also tested in the transonic wind tunnel, where time-accurate displacement measurements were performed using laser sensors. The analysis of experiments and numerical simulations shows that transonic flutter is actually a forced response to an unsteady aerodynamic-load, rather than a two-way fluid-structure interaction. Higher natural modes, with a frequency close to the aerodynamic fluctuating pressure, are directly excited. Generally, the additional constraint in the center does not seem to add significant benefits in terms of dynamic stability in the transonic regime. Numerical results also suggest that the pin has a destabilizing effect at medium-low altitudes in the hypersonic regime. Conversely, flutter was successfully delayed in the supersonic regime.

DISTRIBUTION A: Distribution approved for public release.

I. SUMMARY

The report is presented in terms of publications.

1) Currao, G., He, H., *Transonic Flutter of Skin Panels and Performance at Higher Speeds* , AIAA Journal (**Submitted:** 07-Nov-2023, **Status:** Major Corrections)
2) Currao, G., *Transonic Leading-Edge Stall Flutter: Modeling, Simulations and Experiments* , J. of Fl. Mech. (**Submitted:** 13-Sep-2023, **Status:** Accepted/minor revisions)

The main journal article is *Transonic Flutter of Skin Panels and Performance at Higher Speeds*, it has been submitted to AIAA Journal and the topic is exactly what the AFOSR project has paid for. The second journal article is a spin-off work, that however would not have been possible without the instrumentation (high speed camera) that was purchased thanks to the AFOSR project.

II. ACCOMPLISHMENTS OVERVIEW

The aim of the project is to evaluate the aeroelastic characteristics of the floating-panel design at off-conditions in the transonic regimes. In the original project the aim was broken into three research questions.

A. **OBJECTIVE #1** - Evaluation of floating-skin panel design aeroelastic characteristics

   Research question: *Is the presence of posts stabilizing or destabilizing?*

   Completeness level: 100%

   The presence of a central post is stabilizing at high speeds, especially at lower altitudes, but adds little benefits in the transonic regimes.

B. **OBJECTIVE #2** - Optimization of floating-skin panel design to meet low-weight requirements

   Research question: *What is the optimal number of posts to be employed?*

   Completeness level: 30%

   A parametric study in terms of positioning of post has yet to be performed. The numerical results produced so far suggest that the post should not be put in the center to avoid flutter by coalescence of the first two modes.

C. **OBJECTIVE #3** - Global evaluation of aeroshell structural stability at subsonic, transonic, supersonic and hypersonic speeds

   Research question: *Is transonics or hypersonics the worst flight regime?*

   Completeness level: 100%

   A parametric study in terms of altitude and Mach number was conducted for an Inconel steel plate. Thermal effects were included in the calculations. Below Mach 5 and along the air-breathing corridor (q =10 - 150 kPa), the lowest flutter margins were observed int he transonic regime.

DISTRIBUTION A: Distribution approved for public release.

Transonic Flutter of Skin Panels and Performance at Higher Speeds

Gaetano M. D. Currao* & Hsu-Chang He†
National Cheng-Kung University, Tainan City 701, Taiwan R.O.C.

This work is a numerical and experimental study of transonic panel flutter where alternative boundary conditions are explored. Hypersonic vehicles are subjected to strict low-weight requirements, thus skin-panel configurations are often optimized to maximize the payload. In the case of Skylon, a single-stage-to-orbit concept vehicle, one of these configurations involves the use of a series of discrete supports to stiffen thinner skin-panels, thus the question arises of whether this configuration offers improved stability margins also in the transonic regime. The geometrical boundary conditions are herein idealized as a rectangular panel clamped on all sides and with a rigid pin located in the middle. A numerical parametric analysis was conducted for a steel skin-panel for a range of altitude and Mach numbers to quantify the benefits of this panel configuration in the transonic, supersonic and low-hypersonic regime. A panel clamped on all sides and with a pin in the center was also tested in the transonic wind tunnel, where time-accurate displacement measurements were performed using laser sensors. The analysis of experiments and numerical simulations shows that transonic flutter is actually a forced response to an unsteady aerodynamic-load, rather than a two-way fluid-structure interaction. Higher natural modes, with a frequency close to the aerodynamic fluctuating pressure, are directly excited. Generally, the additional constraint in the center does not seem to add significant benefits in terms of dynamic stability in the transonic regime. Numerical results also suggest that the pin has a destabilizing effect at medium-low altitudes In the hypersonic regime. Conversely, in the supersonic regime flutter was successfully delayed.

Nomenclature

C_v,C_p	=	constant volume and pressure specific heat coefficients, J/kg/K
h	=	altitude, m
k	=	specific turbulence kinetic energy, m^2/s^2
F_1	=	blending function in the k-ω SST model

*Assistant Professor, currao@gs.ncku.edu.tw
†Master Student

DISTRIBUTION A: Distribution approved for public release.

f	=	frequency, Hz
L	=	transition length, m
L_p	=	modified transition length, m
M	=	Mach number, dimensionless
P	=	pressure drop, dimensionless
p	=	pressure, Pa
q	=	dynamic pressure $\gamma p M^2/2$, Pa
r	=	recovery factor, dimensionless
Re_∞	=	freestream Reynolds number, m^{-1}
Re_x	=	local Reynolds number, dimensionless
S	=	boundary layer separation point, m
T	=	temperature, K
u	=	velocity, m/s
w	=	normal displacement, m
x	=	streamwise distance from LE, m
y	=	spanwise coordinate, m
α_D	=	Rayleigh mass-coefficient, dimensionless
α_T	=	thermal expansion coefficient, dimensionless
α, $\alpha*$	=	k-ω closure coefficients, dimensionless
β, $\beta*$	=	k-ω closure coefficients, dimensionless
β_D	=	Rayleigh stiffness-coefficient, dimensionless
γ	=	specific heat ratio, dimensionless
Δx	=	cell length, m
Δy	=	cell height, m
ΔL	=	variation in L , m
Δp	=	variation in p , Pa
θ_w	=	wedge angle, deg
μ	=	viscosity, Pa s
ν	=	Poisson coefficient, dimensionless
ρ	=	density, kg/m^3
σ_k, σ_ω,σ^*	=	k-ω closure coefficients, dimensionless
τ	=	shear stress, Pa

DISTRIBUTION A: Distribution approved for public release.

τ_{ij} = shear-stress tensor, Pa

ω = specific dissipation rate, s^{-1}

ω_1, ω_2 = natural circular frequency $f \times 2\pi$, rad/s

Subscripts

1,2,3 = frequency relative to the corresponding natural mode

CFD = relative to numerical simulation

E = just upstream of the expansion-wave impingement-point

FEM = relative to modal structural analysis

I = at the inviscid shock-impingement point or at the corner

L = relative to laminar solution

r = recovery

T = relative to turbulent solution

w = at the wall

∞ = freestream

Abbreviations

CFRP = carbon fiber reinforced polymer

FSI = fluid-structure interactions

LE = leading edge

LS1,LS2,.. = laser sensor name

IR = infrared thermography

PT = pressure transducer

PSP = pressure-sensitive paint

TPS = thermal protection system

I. Introduction

Hypersonic cruise vehicles are designed to accelerate through low-speed regimes to reach the design altitude and speed. However, because of their inherently low propulsive and aerodynamic efficiency, high-speed vehicles are subjected to strict low-weight requirements [1]. Additionally, the high heating loads characterizing hypersonic flows negatively impact material mechanical properties, thereby further reducing the effective stiffness of skin-panels. Consequently, panel thickness, material and thermal protection systems (TPS) have to be optimized to maximize the payload while ensuring structure integrity.

DISTRIBUTION A: Distribution approved for public release.

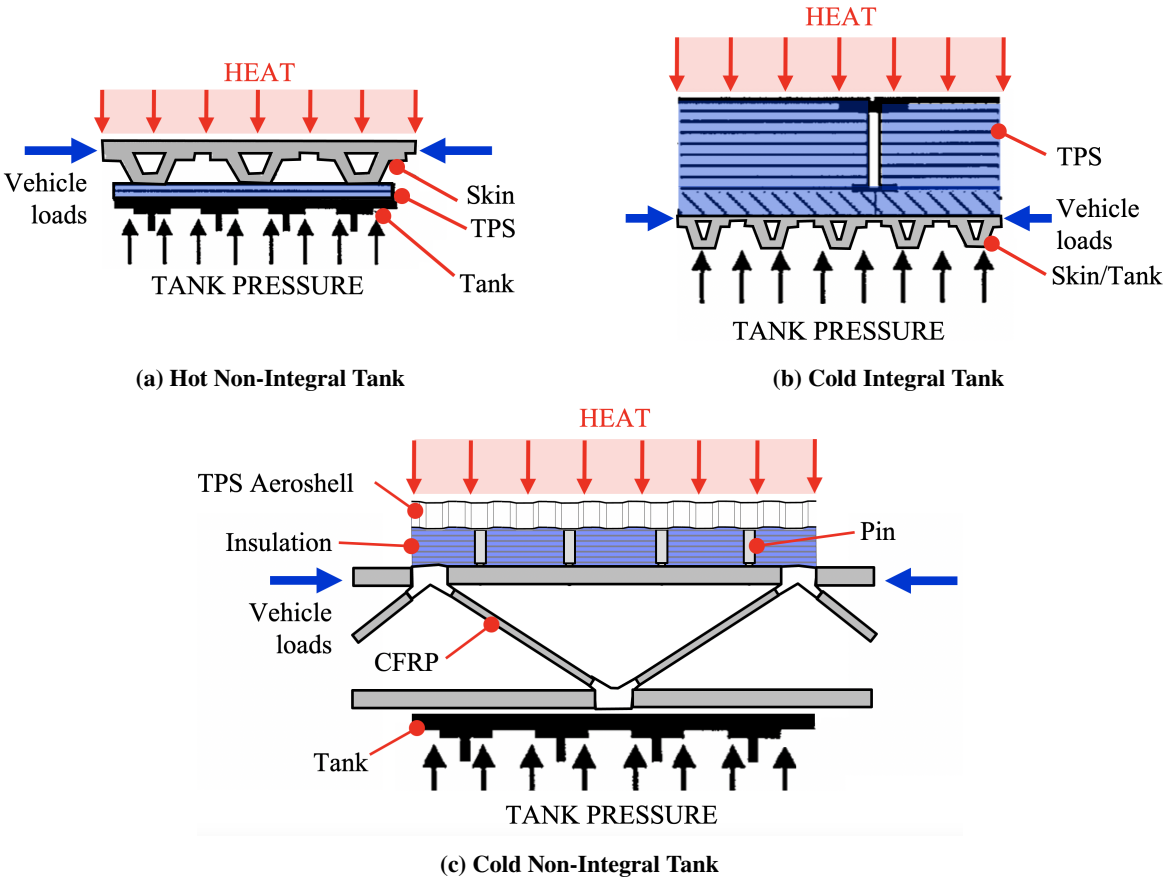

Fig. 1 Schematics of different structure approach concerning the positioning and use of thermal protection system, load bearing structure and tankage (redrawn and readapted from T.J. Bogar and McClinton [2] with elements from Varvill and Bond [3])

Figure 1 shows various structural design approaches to minimize vehicle weight. In the *hot non-integral* type (1(a)) the load bearing structure is directly exposed to thermal loads. As the name suggests, a *non-integral tank* does not contribute to structure integrity, thus this allows for small tank pressure and consequently thinner tank walls. For hypersonic flight, a cold integral approach (Fig. 1(b)) is usually preferred because it generally allows for larger thermal loads while ensuring better packaging and a smaller volume [2]. With this design, the TPS transfers the aerodynamic load to the tank which is also the supporting structure. Generally, however, higher tank pressures are necessary to maximize the payload. It is also very important that the entire aerodynamic load is completely transferred to the load-bearing structure, a task accomplished through the use of insulating glue such as in the case of the space shuttle[4]. An approach employed in single-stage-to-orbit (SSTO) vehicle designs, such as HOTOL and Skylon, is that of cold non-integral tanks [5, 6]. As shown in Fig. 1(c) the load-bearing structure is decoupled from the thermal shield panels. The panel structure is typically composed of an outer shield, the TPS, which has to sustain the thermal loads while transmitting the aerodynamic load to the underlying structures. This strategy allows for the use of ultra-light materials, such as carbon fiber, for the load bearing structure [3]. Insulation layers

DISTRIBUTION A: Distribution approved for public release.

located underneath the TPS will protect the inner structural components from high thermal loads. In the first design from Varvill and Bond [3], the TPS is a corrugated reinforced glass ceramic panel that is pinned to the carbon fiber truss system through a series of local supports or *pins*. The aeroshell mainly protects against the heating and sustains the local aerodynamic loads, while the vehicle inertial-loads are absorbed by the carbon fiber truss structure. This allows for lower tank pressure, because the oxygen cryogenic tank does not have to provide structural support[3].

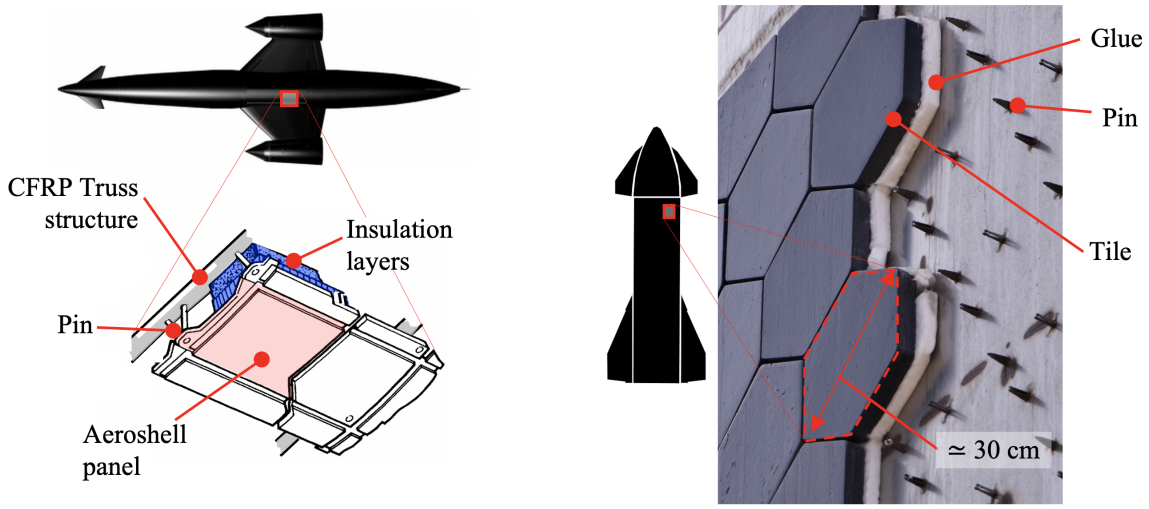

(a) Skylon **(b) Starship**

Fig. 2 Examples of TPS configurations involving local pins on (a) Skylon [3] and (b) Starship (redrawn and readapted from a twitter post: @Cooper_Hime Mar 9, 2021)

Skylon TPS is different from previous or current designs. As mentioned above, the space shuttle tiles were glued directly on the vehicle fuselage typically through the use of silicon adhesive; the TPS were thick highly-porous silica blocks that virtually completely shielded the internal environment from the thermal loads[4]. A different approach is used on Starship, as shown in Fig. 2(b). Large 30 cm wide hexagonal tiles are pinned to the vector fuselage. Between tiles and steel skin, a foam is used to provide thermal insulation as well as greater adherence. This design allows for minimal tiles movement, thus dissipating internal stress due to the steel-fuselage thermal expansion. In Skylon (Fig. 2(a)), the aeroshell has to be connected to the carbon fiber truss through the use of spaced local supports or pins. However, the design of SSTOs is different from multistage-to-orbit vehicles, as hypersonic air-breathing vehicles are designed to reach hypersonic speeds within the atmosphere [7]; consequently the largest thermal loads are experienced during the ascent, where TPS is required to resist thermal loads in excess of 1000 K .

While these structural solutions are optimized for hypersonic regimes, it is necessary to evaluate structural stability in the transonic regime, where flutter margins are typically at a small [8]. From an aeroelastic perspective, the hypersonic

DISTRIBUTION A: Distribution approved for public release.

regime differs from the supersonic regimes with regards to mechanical properties degradation induced by large heating levels. In the cases where thermal degradation is not a dominant factor, for example of Mach < 5 and temperature resistant material, is hypersonic or transonic the most critical regime in terms of structural dynamic stability? Answering this question is especially critical for long vehicles (length > 20 m), such as the SSTOs, as the presence of a curved body near the nose of the vehicle and at aft length could significantly reduce the critical Mach number. However, research on off-design conditions for hypersonic aircraft is rare, with significant contributions to the field by Küchemann [9] and Bowcutt [10].

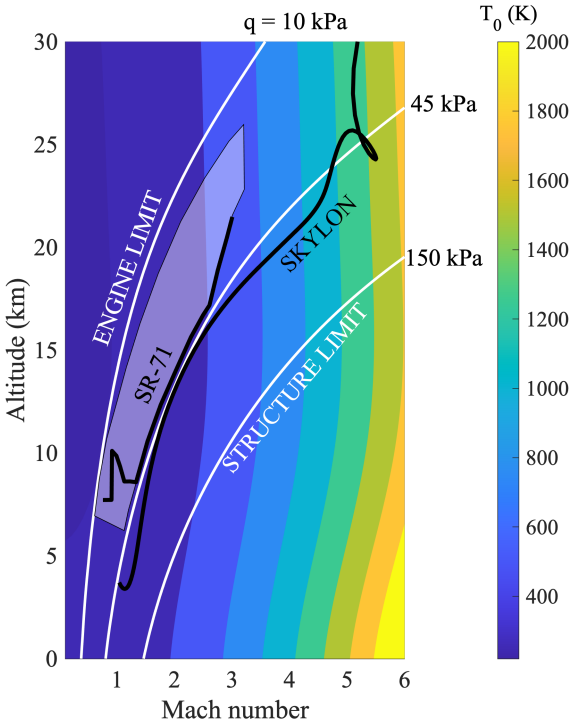

Fig. 3 Trajectory for SR-71[11] and Skylon[12].

During the early ascent stages, the lift-to-drag ratio of SSTOs is critically below the designed cruise level. An example is the only air-breathing aircraft capable of reaching speeds in excess of Mach 3; the SR-71 was designed to perform a dive at about 10 km altitude to rapidly cross the transonic regime and accelerate towards cruise conditions [11], as shown in Fig. 3. As a result, the skin panels are expected to experience a rapidly changing flow from subsonic to supersonic speeds. To investigate this effect, Shishaeva et al. [13] proposed an off-design study of 2D skin panels subjected to accelerating and decelerating flow. Between Mach 0.8 and 1.7 it was possible to identify approximately seven types of instabilities, with rapidly changing speeds shown to result in attenuation of flutter. Rapid changes in altitude, such as during the transonic dive, will generally affect the pressure differential between the external

DISTRIBUTION A: Distribution approved for public release.

flow and the internal aircraft environment, often referred to as cavity pressure. As shown by G.A. Davis [14], the pressure differential generally results in a stiffening of the panel and determines whether the panel mean deformations will be towards the flow or cavity side; In the former case, transonic flutter is promoted by the creation of a stronger shock.

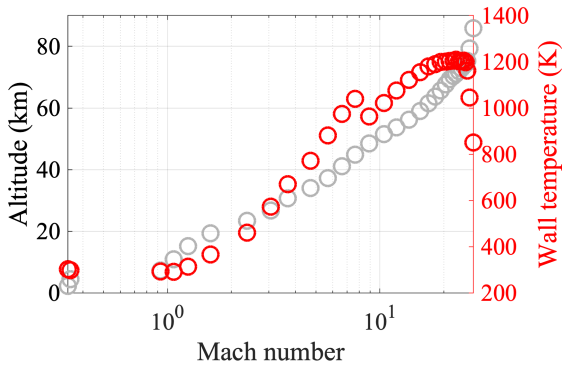

Fig. 4 Temperature measurements performed on space shuttle tiles during the last phase of re-entry (data retrieved from Gong et al. [15]).

During the descent phase, skin-panels might exhibit reduced mechanical properties due to the high temperatures experienced at higher altitudes. Fig. 4 shows the temperature on the tiles of the space shuttle right-wing, which was recorded through infrared thermography during the descent phase [15]. The temperature (red data) is shown as a function of both altitude (gray data) and Mach number. At Mach close to one, there is still a residual wall temperature close to 300 K. Whether it is possible to achieve a similar amount of heat dissipation with less refractive material, such as inconel steel, is not completely clear. Upon reentry from a Mach 3+ cruise, ground crew had to wait for the body of the SR-71 to cool down before approaching the aircraft, as the skin temperatures exceeded 570 K [16]. From this it is conceivable that, during the transonic phase of the descent, the skin-panel residual temperature could have been higher than that measured on the ground. In addition, the panel temperature distribution is generally very non-uniform. Besides experimental attempts towards recreating a realistic thermal distribution on flat plates [17, 18], numerical studies generally assume panels with uniform temperatures. To understand this behavior, Bhatia and Beran [19] conducted a study of thermally stressed panels undergoing transonic flutter, showing that in-plane thermal stress causes a stiffening of the panel, thus delaying flutter. However, the actual thermally buckled shape was not considered in the aerodynamic model, and the question remains of whether material property degradation would play an important role in terms of dynamic instability.

This scenario is further complicated by the strong non-linear characteristics of transonic fluid-structure interactions, which is also present for small vibration amplitudes [14]. For this reason, a time-accurate approach is often preferred to frequency-based methods. The latter typically consist of modal superposition of harmonic loads [20], making it

DISTRIBUTION A: Distribution approved for public release.

is accurate for only small shock oscillations around the static-steady position. Conversely, time integration methods are simpler to implement and allows for the shock to disappear for small deflections [21]. Time-based calculations, however, involve a significantly higher computational cost. Nonetheless, by applying a few mathematical reformulations, it is possible to use frequency-based methods, especially for panel flutter problems where the largest deformation can be of the order of the panel thickness, thus small in absolute terms. Timme et al. [22], for example, expressed the external aerodynamic loading in terms of structural modes of deformations using a kriging-based approach. Solving the resulting non-linear eigenvalue problem allows to very accurately identify flutter mode and frequency, as well as other unstable modes [23]. To obtain a similar level of accuracy, time-based methods require long simulation time and small time-steps, which is typically too computationally expensive.

As it can be concluded form all the work discussed above, the great majority of the panel-flutter studies in the transonic regimes are typically focused on two-dimensional geometries. This has multiple benefits in terms of computational cost and simplification of the aerodynamic model but most importantly it allows for the isolation of the main driving phenomena characterizing the fluid-structure interaction. Since a low aspect ratio delays the occurrence of flutter, two-dimensional predictions represent a worst case scenario. Concerning the empirical evaluation of transonic flutter boundaries, experimental data are scarce and often challenging to reproduce, especially if 2D solvers are employed. Among the limited data available it is worth mentioning the experimental work of Muhlstein et al. [24], which involves panel-flutter experiments in a transonic wind-tunnel with a test section size of approximately 230 mm $\times$ 460 mm. Special attention was given to reset the boundary layer ahead of the panel deviating the wall boundary layer below the model using a retractable splitter plate. Using a 3D FSI solver, Alder [25] successfully matched the stability boundary for a panel with an aspect ratio of two, reporting only a $\pm 10\%$ disagreement. This work however raises the question of validity of 2D simulations, especially since the intrinsically enhanced flow three-dimensionality of the experiments.

The present work is mainly focused on simulating transonic panel flutter experiment, including wall interference. Referring to Fig. 5, two boundary conditions are explored, namely clamped on all sides (or *clean*) and clamped on all sides with a pin in the center. The panel has a length of 330 mm and a span-to-length aspect ratio of 1.5. The formulation of the numerical technique is introduced in Sec. II. The parametric numerical study conducted in Sec. III aims at determining possible improvements in stability margins when a pin configuration is used. To that end, a series of simulations are performed at different Mach numbers and altitudes for the two panel configurations. Sec. IV describes the experimental set-up, material properties evaluation as well as the flow characterization technique in the transonic wind-tunnel. The numerical predictions are used to interpret and analyze the experimental data in Sec. V. Conclusions are drawn in Sec. VI.

DISTRIBUTION A: Distribution approved for public release.

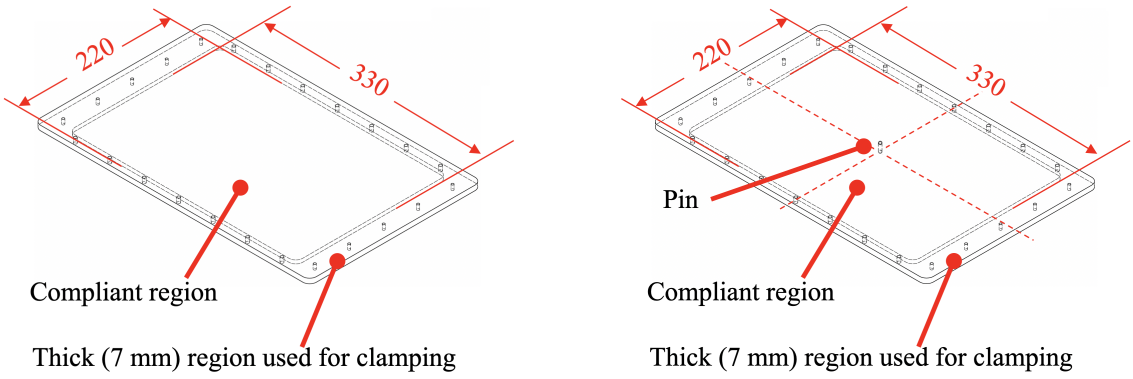

(a) Clean **(b) With pin in the center**

Fig. 5 Details of geometry and boundary conditions explored within this work

II. Numerical technique

The FSI numerical simulations were computed by coupling the fluid solver with the structural solver at every time step $\Delta t = 0.1$ ms (*i.e.* two-way coupling). The commercial software ANSYS/Fluent was used to solve the 3D transient Navier-Stokes equations, which can be expressed as follows:

$$\frac{\partial \rho}{\partial t} + \frac{\partial (\rho u_j)}{\partial x_j} = 0 \tag{1}$$

$$\frac{\partial (\rho u_i)}{\partial t} + \frac{\partial (\rho u_i u_j)}{\partial x_j} = -\frac{\partial p}{\partial x_i} + \frac{\partial \hat{\tau}_{ji}}{\partial x_j} \tag{2}$$

$$\frac{\partial (\rho E)}{\partial t} + \frac{\partial (\rho u_j H)}{\partial x_j} = \frac{\partial}{\partial x_j}\left(u_i \hat{\tau}_{ij} + (\mu + \sigma^* \mu_T)\frac{\partial k}{\partial x_j} - q_j \right) \tag{3}$$

where μ is the molecular viscosity and $\hat{\tau}_{ij}$ is the total viscous shear stress tensor:

$$\hat{\tau}_{ij} = (\mu + \mu_T)\left(\frac{\partial u_i}{\partial x_j} + \frac{\partial u_j}{\partial x_i} - \frac{2}{3}\frac{\partial u_k}{\partial x_k}\delta_{ij} \right) - \frac{2}{3}\rho k \delta_{ij} \tag{4}$$

$E = (C_v T + u_i u_i/2 + k)$ and $H = (C_p T + u_i u_i/2 + k)$ are the mean total specific energy and enthalpy respectively; the heat flux vector can be written as:

$$q_j = -\left(\frac{\mu}{Pr_L} + \frac{\mu_T}{Pr_T} \right)\frac{\partial C_p T}{\partial x_j} \tag{5}$$

where Pr is the Prandtl number. Adiabatic wall condition is assumed, thus wall heat-flux $q_w = 0$. The equations are coupled with the ideal gas equation for air. Additionally, the $k - \omega$ shear-stress transport (SST) [26] equations are used to calculate the eddy viscosity term μ_T. This turbulence model was chosen because of its good performance in boundary layers as well as in free shear layers. The transport equations of specific turbulence kinetic energy k and dissipation rate ω can be written as follows:

DISTRIBUTION A: Distribution approved for public release.

$$\frac{\partial(\rho k)}{\partial t} + \frac{\partial(\rho u_j k)}{\partial x_j} = P_k(\beta^* \rho \omega k) + \frac{\partial}{\partial x_j}\left[(\mu + \sigma_k \mu_T)\frac{\partial k}{\partial x_j}\right] \tag{6}$$

$$\frac{\partial(\rho \omega)}{\partial t} + \frac{\partial(\rho u_j \omega)}{\partial x_j} = P_k(\beta \rho \omega^2) + \frac{\partial}{\partial x_j}\left[(\mu + \sigma_\omega \mu_T)\frac{\partial \omega}{\partial x_j}\right] + 2\rho(1 - F_1)\sigma_{\omega_2}\frac{1}{\omega}\frac{\partial k}{\partial x_j}\frac{\partial \omega}{\partial x_j} \tag{7}$$

where α,α^* and β are functions of the turbulence Reynolds number $Re_T = \rho k/\omega\mu$ [27]; consequently μ_T can be expressed as $\mu_T = \alpha^* Re_T \mu$. P_k and P_ω are the net production per unit dissipation for k and ω [27]. F_1 is the blending function between the standard $k-\omega$ model ($F_1 \rightarrow 1$, near the wall) and the $k-\epsilon$ model ($F_1 \rightarrow 0$). These equations were numerically solved with an implicit, cell-centered, second-order upwind solver.

$$P_k = \frac{\alpha^*}{\beta^*}\left(\tau_{ij}\frac{\partial u_j}{\partial x_j}\frac{1}{\mu_T \omega^2}\right) - 1, \quad P_\omega = \frac{\alpha\alpha^*}{\beta}\left(\tau_{ij}\frac{\partial u_j}{\partial x_j}\frac{1}{\mu_T \omega^2}\right) - 1 \tag{8}$$

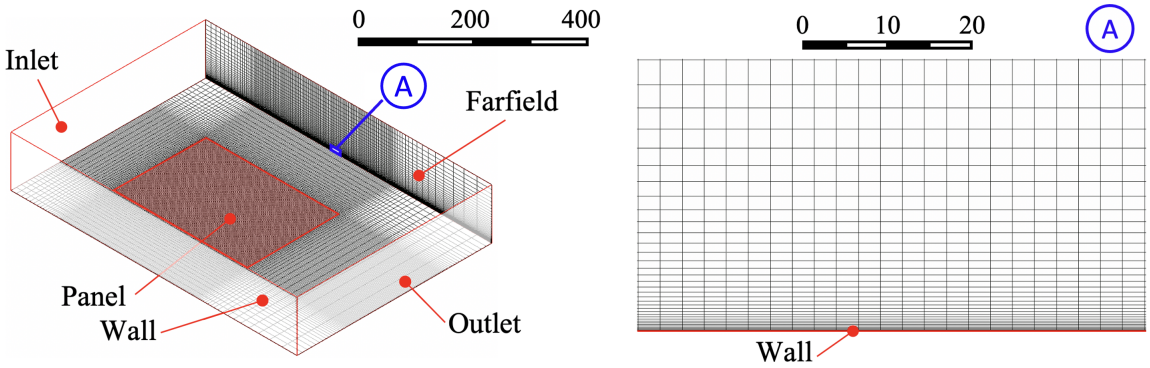

Fig. 6 Details of the simplified mesh (approximately one million of cells) used to establish the flutter margins in Sec. III (size in mm).

The discretized domains used within this work are given in in Fig. 6 and 8. Two types of mesh are used; the simplest, shown in Fig. 6, which will be referred to as the *ideal domain* (330 mm × 890 mm × 1320 mm) with more than a million cells. Figures 7(a-b-c) show the mesh independence studies for the ideal domain at $M = 0.98$, 3.5 and 5 along a $q = 45$ kPa trajectory. The total shear-stress force acting on the panel is used as the reference index to establish if mesh independence is achieved. The solid data point is the reference mesh, with a minimum cell height of $\Delta y = 0.1$ mm at the wall. At Mach 5 a different reference mesh with $\Delta y = 0.025$ mm was also considered. Generally, a one million cells mesh, with a minimum cell length and height of 2 mm and 0.1 mm respectively, ensures a reasonable level of accuracy with an error below 5%. In terms of boundary conditions, the plane adjacent to the panel is set to viscous wall, while the other five enclosing planes are non-reflective boundaries or farfields. This domain will be used for the FSI calculations in Sec. III to approximately establish the flutter margins of the two skin-panel configurations in terms of altitude and Mach number at cruise. In addition, the experiment is simulated using the mesh shown in Fig. 8, that includes both the wind-tunnel model and the test section geometry (600 mm × 600 mm × 1200 mm). The high-fidelity mesh has the same level of

DISTRIBUTION A: Distribution approved for public release.

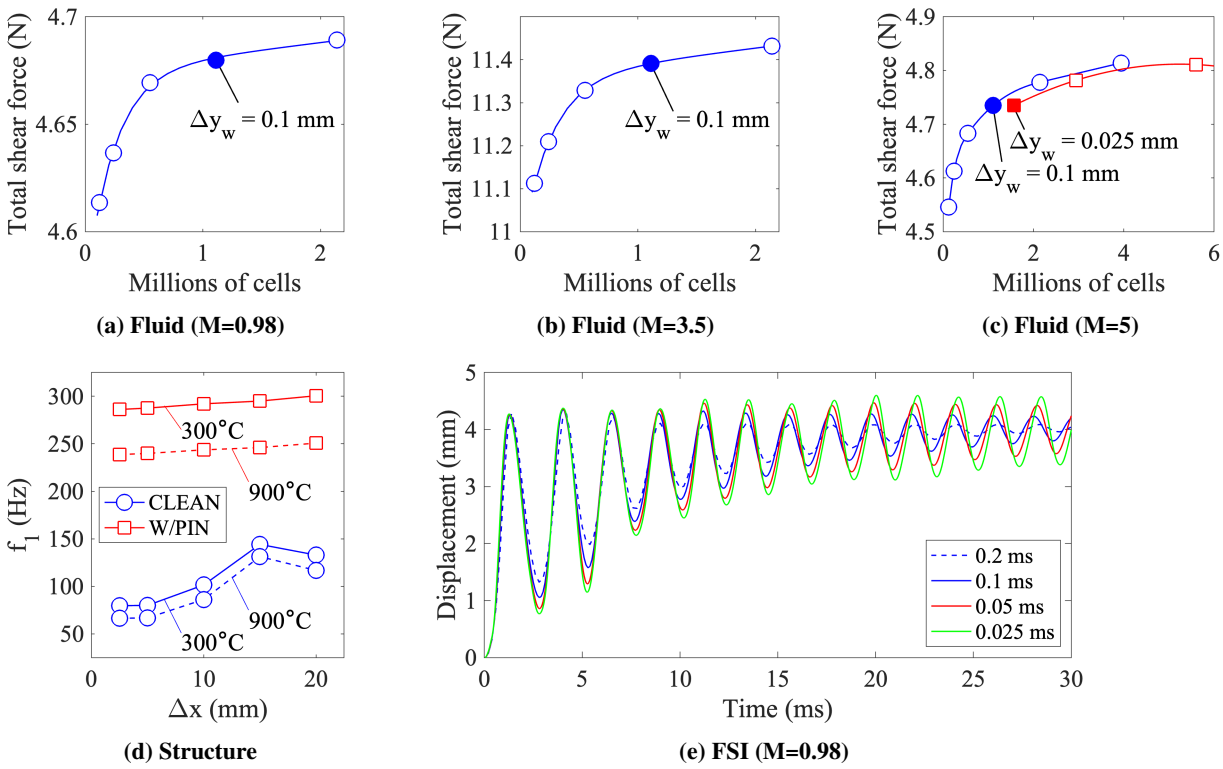

Fig. 7 Mesh and time independence study: (a-b-c) mesh refinement of fluid domain for q = 45 kPa, (d) mesh refinements for the shell at different wall temperatures and (e-f) time independence study for the FSI simulations.

refinement as the ideal mesh, yielding a total cell count larger of more than ten million cells. During the coupling process, nodal displacements are retrieved from the FEM solver and applied to the mesh. Smoothing techniques were employed to maintain the mesh density of the boundary-layer, while diffusing all the residual mesh deformations away from the wall.

The structure is a rectangular plate with a chord of 100 mm and a span of 200 mm, with a converged cell-size of 2.5 mm. The mesh independence study for the structure side are conducted in Fig 7(d) for both the configurations (clean and with central pin) at room temperature and at $T_w(x, y) = 900°$. The maximum plate thickness employed was 2.2 mm, thus a shell element type was employed, which is a 3D 8-node membrane with six nodal degrees-of-freedom. The materials considered are linearly elastic and isotropic. Referring to the governing equation in the finite-element model (FEM) formulation:

$$[M]\ddot{w} + [C]\dot{w} + [K]w = f \tag{9}$$

w is the nodal displacement vector, f represents nodal loading while M, C, K are mass, damping and stiffness matrices respectively. The Rayleigh damping model [28] was employed to calculate $C = \alpha_D M + \beta_D K$ based on the first two

DISTRIBUTION A: Distribution approved for public release.

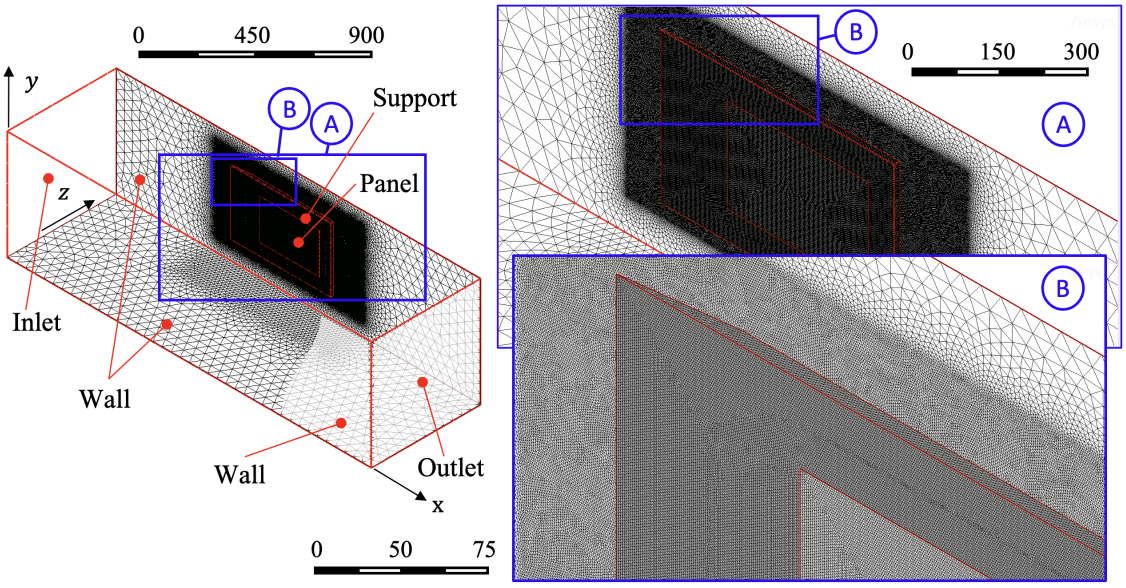

(a)

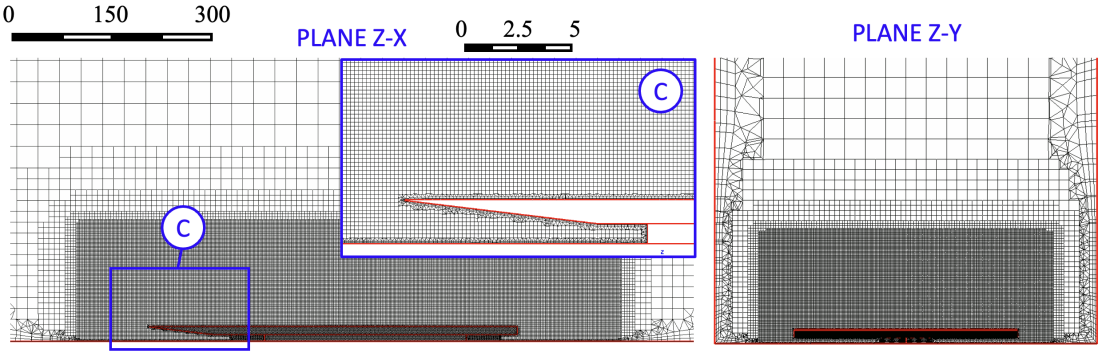

(b)

Fig. 8 Details of the high-fidelity mesh used to simulate the experiment in Sec. V (approximately ten millions cells).

natural circular frequencies as follows:

$$\alpha_D = \frac{2\omega_1\omega_2}{\omega_2+\omega_1}\zeta \quad \beta_D = \frac{2}{\omega_2+\omega_1}\zeta \tag{10}$$

where ζ is the damping ratio. The coupling time-step is set equal to the marching time-step of fluid and structure solver. The time independence study for the coupled simulations is shown in Fig. 7(e). In general, a coarser time-step underestimates the oscillation amplitude, thereby effectively introducing additional damping. Since a time step of 0.025 ms leads to computationally expensive simulations, the approach taken here begins with the use a 0.1 ms time-steps to isolate few flutter points, and then using a 0.025 ms time-step to more accurately determine the flutter boundaries.

DISTRIBUTION A: Distribution approved for public release.

III. Preliminary considerations

This section aims at answering the question of which regime, low hypersonic or transonic, is more critical in terms of flutter. Using the numerical domain previously introduced as ideal mesh (see Fig. 6), panel flutter calculations are conducted for a range of freestream conditions. The values of Mach number explored are 0.98, 2, 3.5 and 5, while the altitudes considered are between sea level and 25 km. The wall temperature is set to the total temperature, thus a unity recovery factor was applied in all simulations for the sake of simplicity. Since SSTOs will experience the highest structural loads during the ascent, cavity pressure (*i.e.* the pressure acting on the back of the panel) is assumed to be larger than the freestream pressure. In general, even a small amount of pressure differential ($< 2\%$ of p_∞) is sufficient to significantly delay or inhibit flutter. A constant pressure differential of 100 Pa was used to model a conservative case of flutter. The panel is 330 mm long, 230 mm wide with a thickness of 1.25 mm. Width and length were decided to be close to those used for the wind-tunnel experiment. The panel material, Inconel alloy 617, is modeled with temperature dependent properties to improve the accuracy of the predictions. For completeness, some of the material properties are provided in Table. 1

Table 1 Inconel Alloy 617 properties (see reference [29])

ΔT (K)	298.15	373.15	473.15	773.15	1273.15
ρ (kg/m^3)	8360	-	-	-	-
E (GPa)	211	206	201	181	139
ν	0.30	0.30	0.30	0.30	0.31
α_T (μ m/m)	0	11.6	12.6	13.9	16.3

A. Flutter margin

Figure 9 shows a summary of all the calculations in terms of altitude, Mach number and wall temperature. Every data point represents a time-based FSI simulation, with a physical time of 0.3 s and a time-step of 0.1 ms. Each simulation takes 96 hours using a single node of 40 cores. To explain the flutter margins for the two configuration, it is necessary to explain the effect of altitude, Mach number and wall temperature. An increase in altitude results in a decrease in density, which reduces the aerodynamic pressure and consequently delays the onset of flutter. The opposite is true for Mach number as $q = \gamma p M^2/2$. Temperature increase can have both beneficial and detrimental effects. While mechanical properties degradation due to thermal loads reduces the effective stiffness of the panel, a buckled panel is less prone to flutter. Referring to the clean configuration (Fig. 9(a)), flutter is present for altitudes below 5 km. However, for Mach number greater than $M \simeq 3$, beneficial buckling effects prevail over the detrimental effects of material properties degradation and increase in aerodynamic pressure. This, however, is not true indefinitely, as degradation of material properties becomes dominant for larger Mach numbers. At Mach 5 and altitude of 15 km, the panel undergoes flutter

DISTRIBUTION A: Distribution approved for public release.

because, while the aerodynamic pressure decreases, the stabilizing buckling effect is smaller. Flutter is absent at higher altitudes.

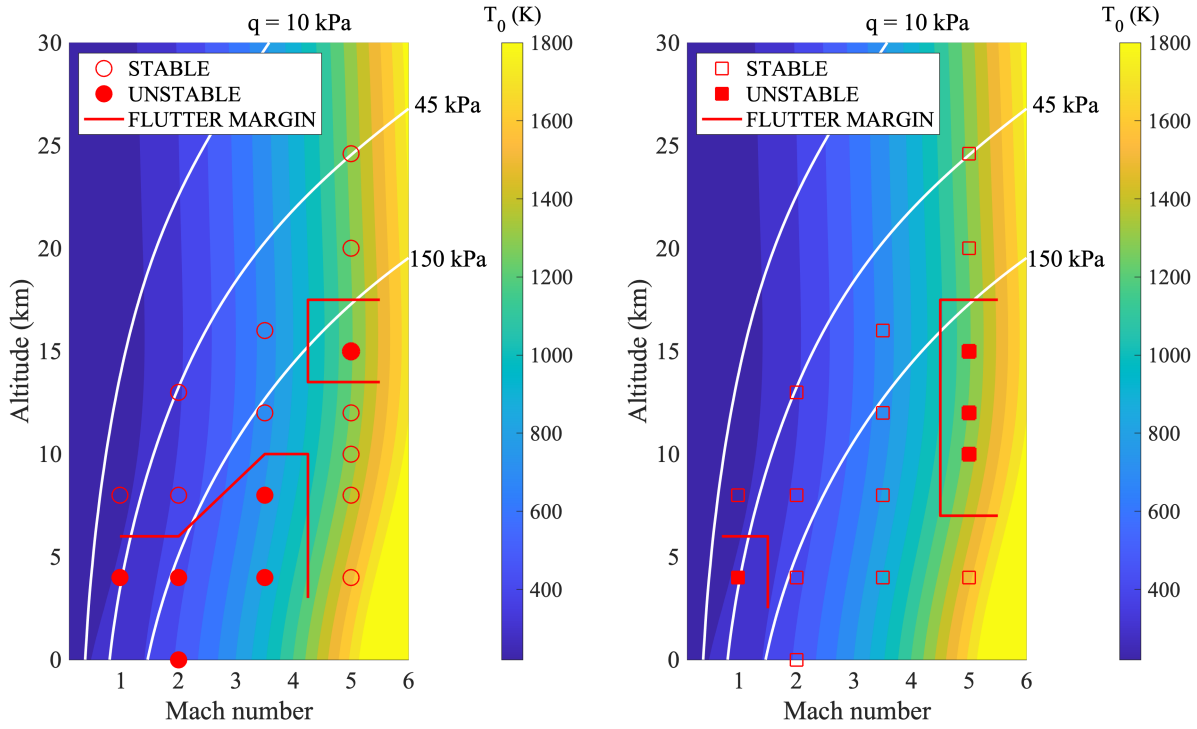

Fig. 9 Summary of the flutter simulations results for the two configurations (Inconel alloy - ideal domain)

The scenario is a bit less intuitive for the configuration with the central pin in Fig. 9(b). The presence of the pin further constrains the panel, which becomes stiffer, thus making it more stable under both static and dynamic conditions. Despite the near overlap of the first and second frequency modes (f_1 = 230 Hz, f_2 = 242 Hz) compared to the clean configuration (f_1 = 64 Hz, f_2 = 102 Hz), the pin's stabilizing effect delays the onset of flutter. Surprisingly, however, the panel undergoes flutter at M =5 only at altitudes between 8 km and 20 km. Below 8 km, buckling inhibits the onset of flutter, very similarly to what happens for the clean configuration. At very high altitudes, the decrease in density is such that the aerodynamic pressure is significantly below the critical value. However, at an intermediate altitude range, the pin constrains the maximum deformation induced by thermal buckling thus promoting the occurrence of flutter.

B. Types of flutter

Referring to the flutter margins previously calculated, Fig. 10 shows panel oscillations amplitude and frequency at selected cruise conditions and altitudes. At M = 0.98 and h = 4 km (Fig. 10(a-b)) the amplitude is of the order of

DISTRIBUTION A: Distribution approved for public release.

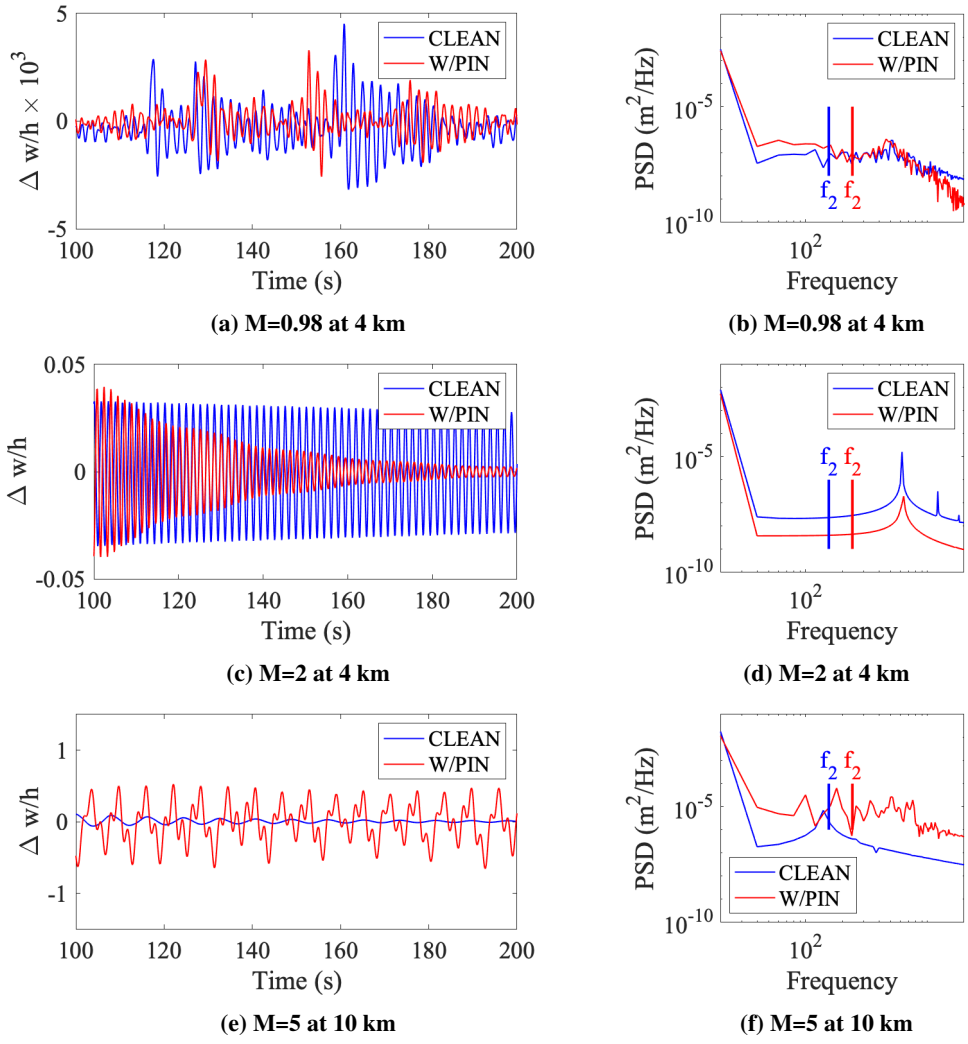

(a) M=0.98 at 4 km **(b) M=0.98 at 4 km**

(c) M=2 at 4 km **(d) M=2 at 4 km**

(e) M=5 at 10 km **(f) M=5 at 10 km**

Fig. 10 Amplitude and frequency spectrum of panel displacement in the transonic, supersonic and hypersonic regimes. Query location at 25% of length and 75% of width. (Inconel alloy - ideal domain)

micrometers, thus three orders-of-magnitude smaller than the panel thickness. The pseudo sinusoidal trend is similar for both configurations with and without central pin. As shown, a sudden increase in amplitude is followed by a decay period of the order of 5 to 10 periods. However, these oscillations do not exceed the envelope for fatigue for the panel thickness herein considered. It can speculated that engine-induced vibrations or those induced by other structural components during flight could cause larger panel oscillations. In terms of frequency spectrum, a distinctive peak appears close to the fourth natural frequency ($\simeq 400 - 500Hz$); an aspect that will be further discussed in Sec. V. The case of $M_\infty = 2$, $h = 4$ km is shown in Fig. 10(c-d). The amplitude is approximately two of orders-of-magnitude smaller than the thickness, but larger with respect to the transonic regime. The clean configuration undergoes flutter, while the presence of the pin appears to be stabilizing. Flutter frequency appears to be located at around 600 Hz, thus close to the fourth or fifth natural mode for both the configurations. The scenario for $M_\infty = 5$ and $h = 10$ km shown in Fig. 10(e-f)

DISTRIBUTION A: Distribution approved for public release.

is significantly different with respect ot the previous two cases. The configuration with pin shows pseudo-periodic sustained oscillations with an amplitude of the order of the panel thickness, while the clean configuration is stable. The frequency spectrum in Fig. 10(f) shows that a large spectrum of frequencies contributes to the chaotic oscillating behavior, thus a single flutter frequency is not identifiable.

IV. Experimental set-up and characterization

A. Transonic wind tunnel

The transonic wind tunnel is located at the Aerospace Science and Technology Research Center (ASTRC) of the National Cheng-Kung University (NCKU). This facility can provide a flow with variable Mach number between $M = 0.2$ and $M = 1.4$ and a freestream Reynolds number between of 20×10^6 m^{-1} and 50×10^6 m^{-1}. The total pressure is monitored upstream of the stilling chamber and controlled using a rotary shut-off ball valve and a rotary perforated sleeve stagnation-pressure control valve. The total pressure is approximately 50 psia ($\sim$ 345 kPa), while the high-pressure reservoirs are at a pressure of 5.15 MPa at room temperature. Stagnation temperature is controlled using a thermal mass matrix which allows for a maximum drop in temperature smaller than 10 K during 30 seconds of test time. The dew point is kept at 230 K. The 600 mm square test section is 1.5 m long with a typical test duration varies between 10s and 30s at Mach 1. In this work the freestream Mach number is set to be $M_\infty = 0.8$ ($p_\infty = 116196$ Pa, $Re_\infty = 22.33 \times 10^6$ m^{-1}), which is sufficient to locally create sonic conditions on the model as it will be discussed later.

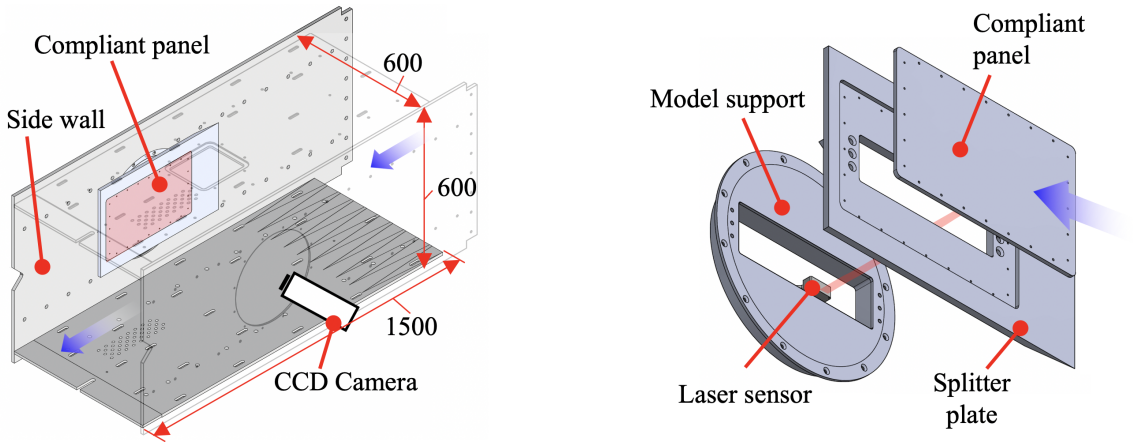

(a) Positioning within the test section **(b) Exploded view**

Fig. 11 Schematics of the wind tunnel model with details of test section and PSP measurement system (size in mm)

B. Wind-tunnel model

Besides a relatively large test section, the wind tunnel model cannot occupy more than 1-2% of the frontal area without causing in blockage. In order to minimize the frontal area, one of the two side windows was removed and

DISTRIBUTION A: Distribution approved for public release.

substituted with the model support, as shown in Fig. 11. The wind tunnel model consists of a compliant panel, a splitter plate and the model support. The test panel is machined out of a block of copper, because of its larger density with respect to aluminum. A smaller stiffness-to-density ratio allows for lower oscillation frequencies and larger displacements, thus increasing the signal-to-noise ratio (SNR) of the laser-based measurements, which will be described in Sec. IV.C. The maximum panel thickness is 7 mm, but the inner complaint region, which is 330 mm long and 220 mm wide, has a thickness of 2 mm. For the configuration with central support, the panel was modified to include a central orifice which was used to support the model using an M5 countersunk screw, as shown in Fig. 12(a-c-e). The panel aspect-ratio was based on the results of a parametric study aimed at maximizing its size, as this would result in larger panel displacement. The splitter plate was manufactured with aluminum, with a leading edge at a distance of 160 mm from the compliant panel so as to have a completely turbulent boundary layer on the compliant region (Fig. 12(d)). The bottom part of the splitter plate is a hexagonal wedge designed to divert the flow around the rectangular cavity. The latter is instrumented with laser sensors and enclosed by a metallic frame, but not hermetically sealed(see Fig.12(c)). Consequently, the cavity pressure rapidly equalizes the test-section pressure within approximately a second of flow.

C. Measurements typology

Displacement measurements were performed using five laser sensors ($\mu - \epsilon$ optoNCDT ILD 1420-25) with a measuring range of 25 mm, a repeatability below 10 μm and a sampling rate of 4 kHz. Pressure measurements were performed only for the static configuration (rigid panel) to characterize pressure uniformity and noise level in the tunnel. Nine pressure transducers (Kulite XCS-093-25A) were located on the panel and one within the cavity. Pressure sensitive paint (UniFIB) was employed to characterize spatial pressure uniformity on the rigid panel. Calibration was performed beforehand using an isobaric chamber where the pressure was gradually increased from approximately 0.75 atm to 1.2 atm. For each value of pressure, the test panel was illuminated using the same UV source employed during the test and at the same distance from the object.

Table 2 Derived material properties for the copper panels

Config.	E (GPa)	ρ (kg/m^3)	ν	η
Clean	85±5	8968	0.34	0.0038
With pin	90±5	8968	0.34	0.0038

D. Panel characterization

The density of the panel was calculated knowing the volume (from drawings) and measuring the weight of the panel, while the Young's modulus was determined by matching the measured natural frequencies with the modal analysis. Figure 13(a-b) shows the power frequency spectrum for the two configurations. This is simply obtained by gently hitting

DISTRIBUTION A: Distribution approved for public release.

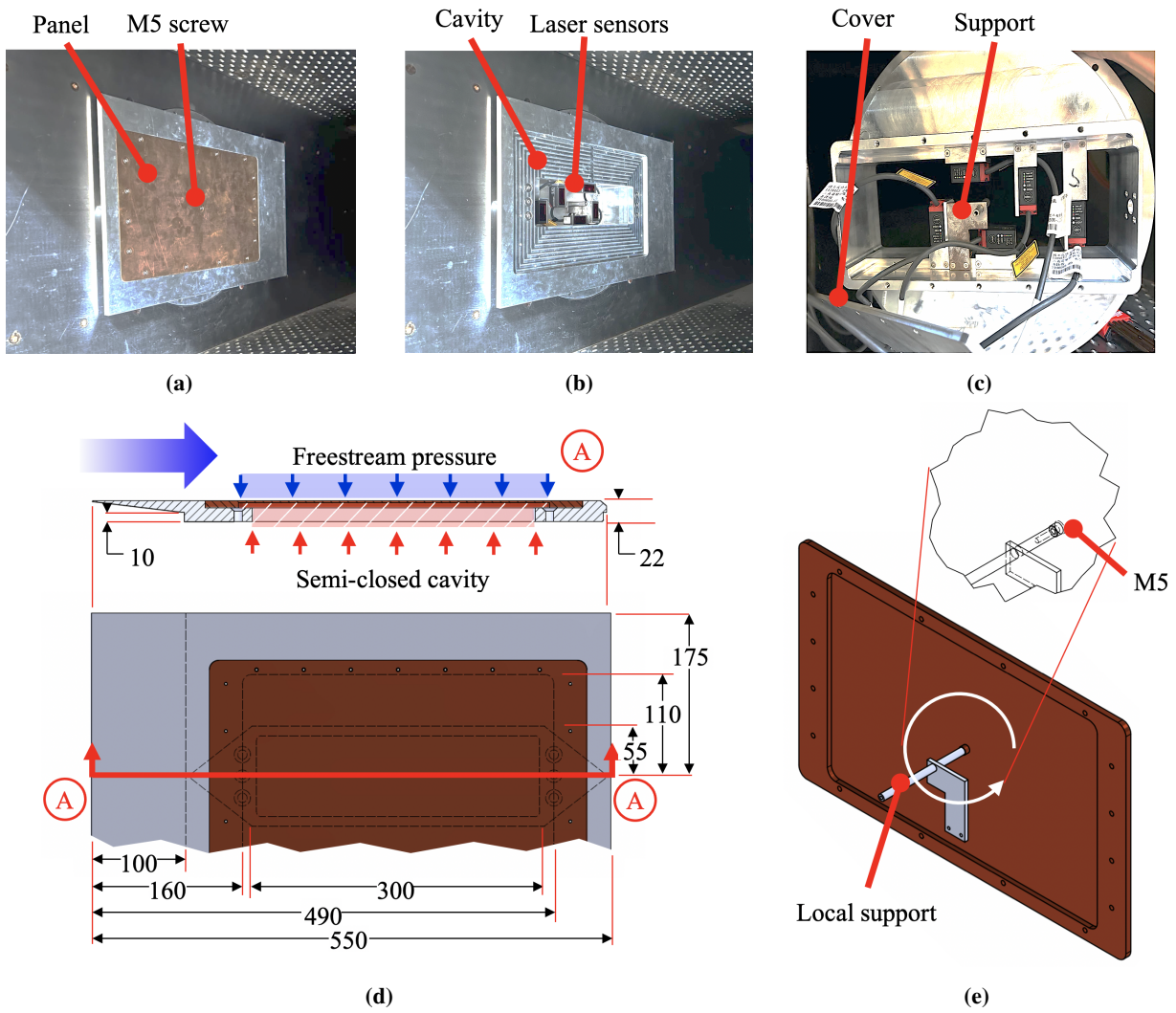

Fig. 12 Photos of the wind tunnel model taken prior the test, dimensions and schematics for the central support (size in mm).

the panel with a light rubber hammer and applying the fast Fourier transform to the measured displacement evolution. Blue data indicates data obtained in the lab while the red data is the result of the frequency tests performed in the tunnel at wind-off conditions. While it is still possible to distinguish the dominant frequencies, the wind-tunnel is typically characterized by a large number of parasite frequencies - likely introduced by each tunnel component such as test-section walls and side bars. Between in-situ and test-bench frequency tests the natural modes appears to be in overall agreement. In order to characterize the panel, it was decided to match the first natural frequency - as it appears in the in-situ tests - trying to minimize the discrepancy with the second natural frequency. Nominal frequencies as well as associated modal reconstruction is shown in Fig. 13(c-d), where the computed natural frequencies present a maximum discrepancy smaller than 10% with respect to empirical values - likely due to thickness non uniformity and residual stresses induced during the machining process. The derived material properties are given in Tab. 2.

DISTRIBUTION A: Distribution approved for public release.

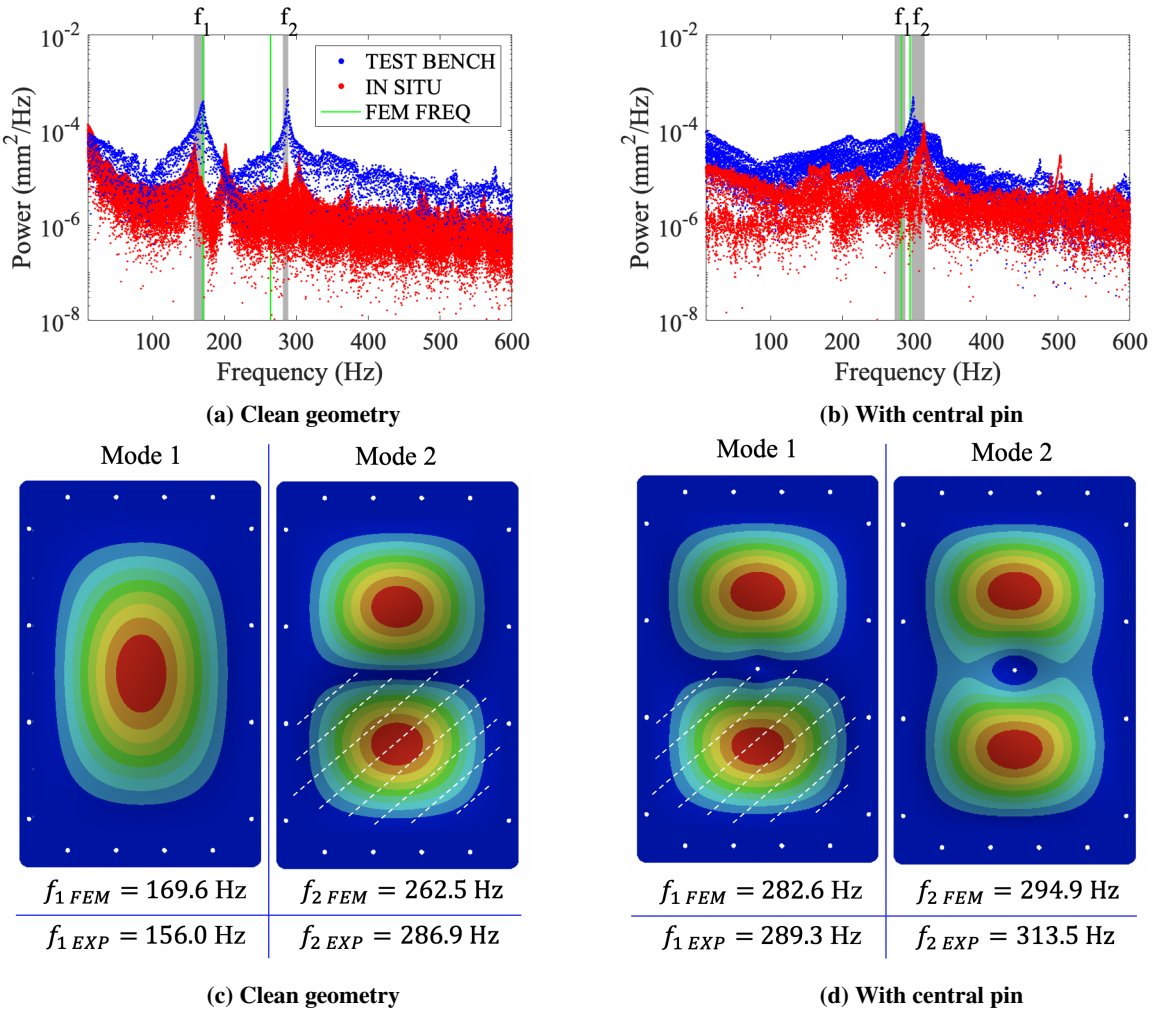

(a) Clean geometry **(b) With central pin**

(c) Clean geometry **(d) With central pin**

Fig. 13 Modal analysis: (a-b) Power spectrum density from experiment and simulation for both configurations (with and without pin) and (c-d) relative modal analysis (dashed region indicates opposite displacement)

E. Flow-field characterization

Although the model is less than 2% of the test-section frontal area, this is sufficient to significantly alter the flow, as it can be seen in the CFD results in Fig. 14(a) where pressure and shear-stress streamline distributions are calculated on the walls and on the wind-tunnel model. Near the leading-edge of the plate, there is a localized region of supersonic flow causing the boundary layer to separate locally and to reattach 10 mm ahead of the panel. On the compliant part of the panel (in red) the streamlines show a small degree of two-dimensionality. The cause of this is that the splitter plate is too close to the side wall of the test section due to the aforementioned blockage restrictions, thus causing a small fraction of the freestream flow to be deflected below the splitter plate. The wind tunnel model causes a local restriction in the test-section causing the flow to become sonic close to the panel, as shown in the Mach number distribution of Fig. 14(b).

DISTRIBUTION A: Distribution approved for public release.

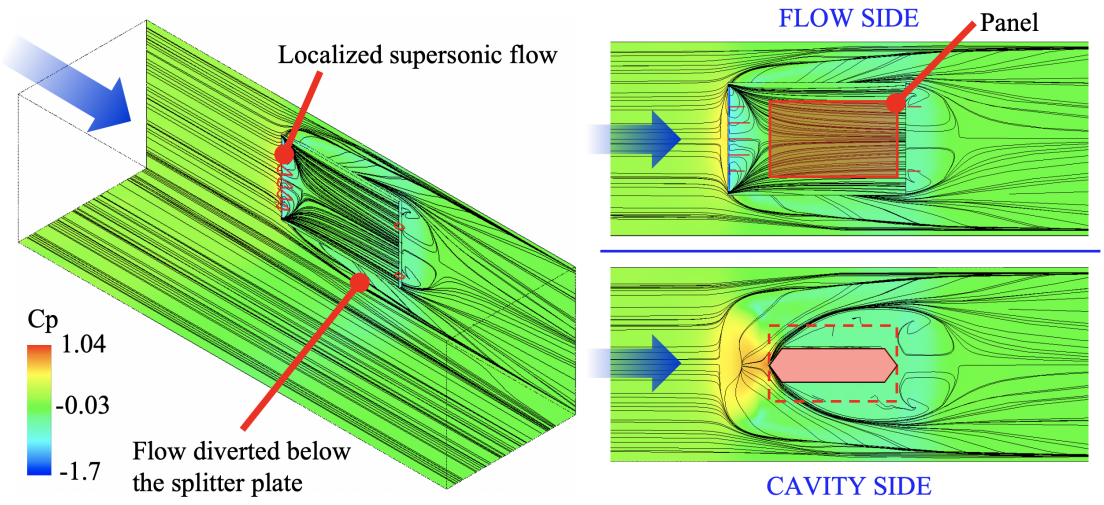

(a) Shear-stress streamlines and pressure distribution on walls and model

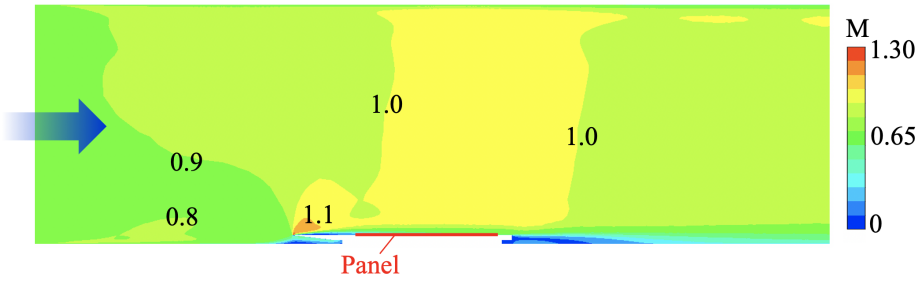

(b) Mach number distribution on symmetry plane

Fig. 14 Steady-state static numerical analysis of the flow-field.

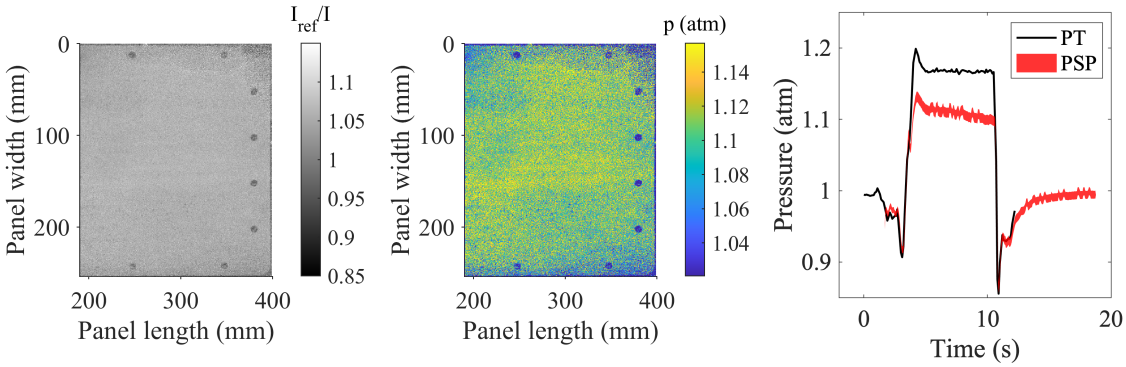

(a) Intensity-ratio distribution **(b) PSP Pressure distribution** **(c) Pressure comparison over time**

Fig. 15 Comparison between pressure transducer and PSP, and measured intensity ratio and pressure distribution (flow is from right to left).

Prior the FSI experiment, static tests were performed and pressure was measured using both pressure transducers and PSP. The latter was applied only on the region that was possible to illuminate and record through the side window

DISTRIBUTION A: Distribution approved for public release.

of the tunnel. Figure 15(a-b) shows PSP intensity and derived pressure distribution, which is relatively uniform with a maximum ±5% variation. A comparison of freestream pressure, as recorded at the end of the convergent nozzle, and the derived average PSP pressure on the panel is shown in Fig. 15(c). The PSP pressure is below the freestream pressure as the wind tunnel model induces a restriction in the test-section inducing an acceleration to approximately sonic conditions. Figure 16(b) shows a comparison between experiment and simulation in terms of pressure distribution along the flow direction over a spanwidth of 80 mm. The pressure here is expressed in terms of pressure differential across the panel, where the measured cavity pressure is p_{cav} = 115.4±5.7 kPa. The best agreement between simulation and experiment are obtained along the centerline. The pressure transducer values that are below the CFD data are slightly below the CFD predictions likely due to wind-tunnel flow angularity, which was previously recorded to be approximately 0.5 degrees [30].

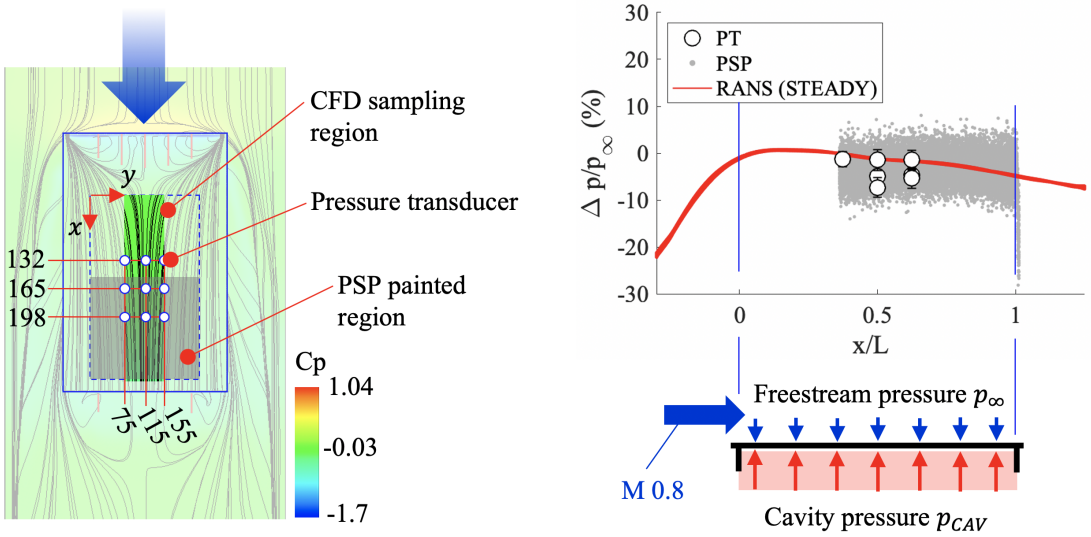

(a) Pressure measurements location (size in mm) **(b) Comparison between CFD and experiment**

Fig. 16 Comparison in terms of pressure between CFD, pressure transducers and PSP.

V. Transonic experiment and simulation

A. Clean configuration

The laser-based measurements of the plate without the pin are shown in Fig. 17. The whole test duration is approximately 10 s, out of which the initial and final transients constitute approximately 5 s. The amplitude of the oscillations is generally of the order of ± 0.1 mm with respect to mean values (in black). Figure 18 offers a 3D visualization of the discrete measurement locations and can be compared with the simulations. The maximum mean displacement is approximately 0.15 mm, and is strongly dependent on the cavity pressure. The numerical results produced here are obtained assuming the nominal value of cavity pressure p_{cav} = 1.156 bar measured a-priori during

DISTRIBUTION A: Distribution approved for public release.

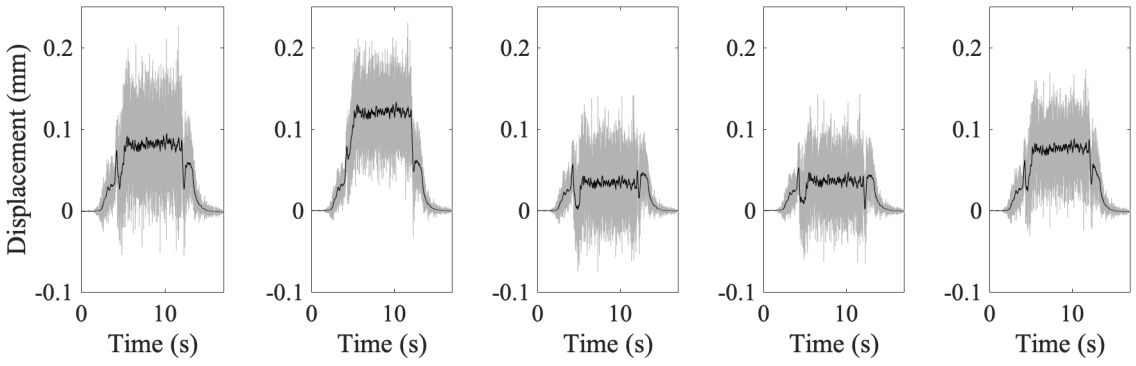

(a) LS1 (0.35L, 0.5W) **(b) LS2 (0.5L, 0.7W)** **(c) LS3 (0.65L, 0.5W)** **(d) LS4 (0.5L, 0.3W)** **(e) LS5 (0.5L, 0.5W)**

Fig. 17 Clean configuration: laser sensors (LS) measurements at a sampling rate of 4kHz with an accuracy of 10 μm. The black line represent the mean value. (Length L = 330 mm, Width W = 220 mm)

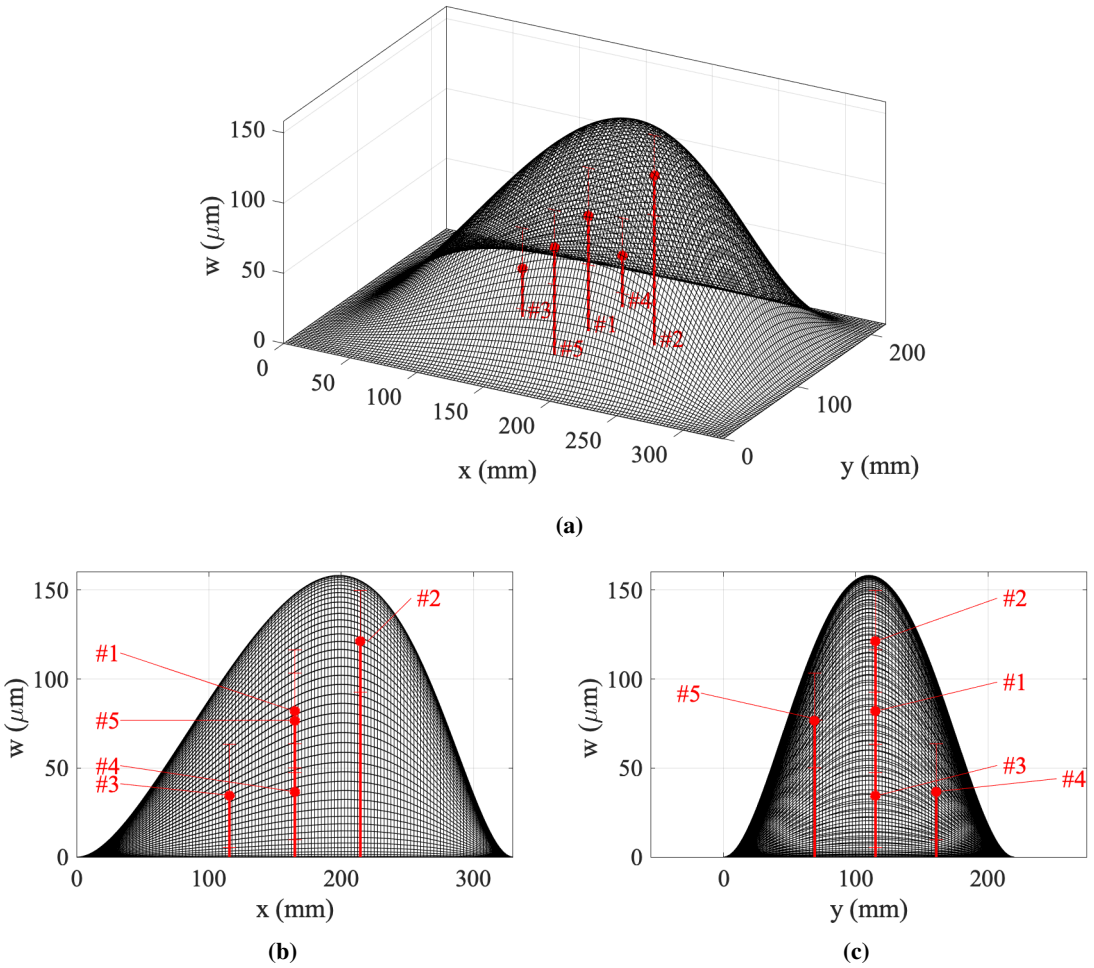

(a)

(b) **(c)**

Fig. 18 Clean configuration: mean and standard deviation of the displacement measured from the laser sensors (in red) with their respective locations, and computed mean displacement distribution.

DISTRIBUTION A: Distribution approved for public release.

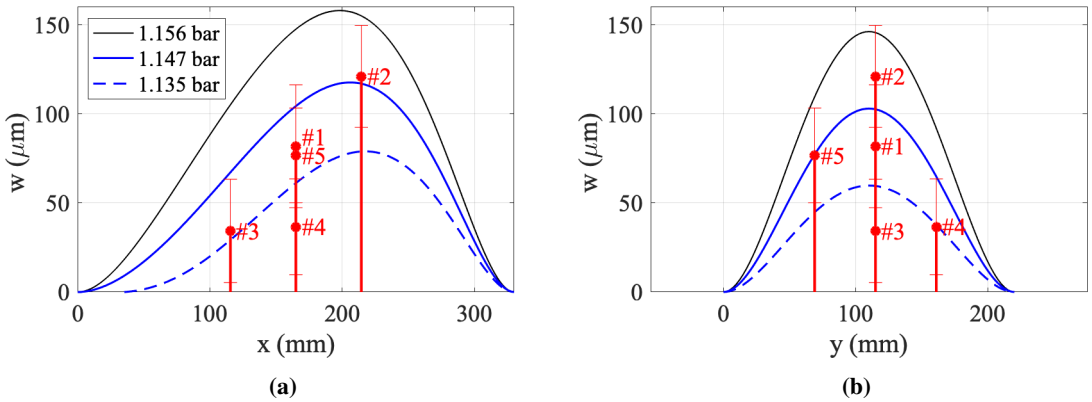

(a) (b)

Fig. 19 Clean configuration: effect of cavity pressure in the simulation final solution and comparison against laser measurements (in red).

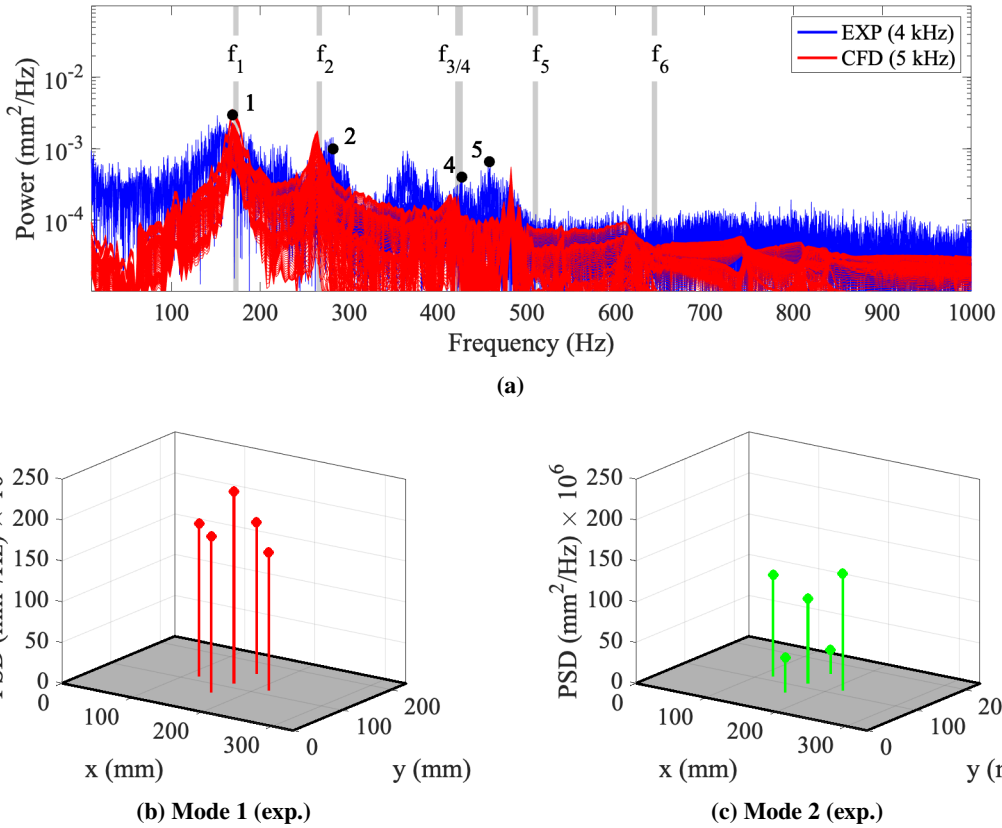

(a)

(b) Mode 1 (exp.) (c) Mode 2 (exp.)

Fig. 20 Clean configuration: (a) Power spectrum density from both laser sensor and simulations at the same query locations and (b-c) first and second power peak distribution.

the static test. In general, the simulation over predicts the empirical measurements by approximately 20 μm. However, a 100 Pa change in pressure differential causes a variation of approximately 8 μm in terms of maximum mean displacement. Additional simulations, for different values of cavity pressure are given in Fig. 19. Here the displacement trend along the two panel symmetry axis is compared against the experiment for multiple values of cavity pressure. As it can be

DISTRIBUTION A: Distribution approved for public release.

seen, the best agreement with the experiment is obtained for a pressure between 1.147 bar and 1.135 bar, which is approximately 0.9% smaller than the measured nominal value of 115.6 bar. The location of the maximum deformation is approximately located between 62 ± 2% of the panel length.

Figure 20(a) shows a comparison of the power density spectrum between experiment and simulation. Some of the peaks are named and will be referenced to in the next section. The first two natural modes are easily identifiable with the peaks 1 and 2, in both simulations and experiment. The power increase between 350 Hz and 400 Hz is speculated to be parasite, *i.e.* the test section is also part of the fluid-structure interaction and structural vibrations are affecting the power spectrum. Peak 4 is weaker and approximately aligned with the third natural frequency; this peak is more easily identifiable in the simulations due to the level of noise characterizing the experiment. An additional peak 5, larger than peak 4, is located at 420 Hz; it appears to be the response of the panel, as it is also present in the simulation. These aspects will be clarified soon, particularly regarding the identification of each peak. For the first two natural frequencies, the maximum power spectrum density is plotted in Fig. 20(b-c), showing a good agreement with the precomputed natural modes (see Fig. 13(c)).

B. Configuration with pin

Similarly to the previous section, Fig. 21 presents the laser-based displacement raw measurements, while Fig. 22 shows a comparison with numerical predictions in terms of both displacement magnitude and location. Generally, simulations agree reasonably well with the sensors for the nominal value of cavity pressure herein considered. Generally, an increase of 100 Pa in cavity pressure causes a change in maximum mean displacement of approximately 3 μm.

Figure 23(a) shows a comparison between experiment and simulation in terms of power spectrum density. For the simulation case (in red), while the two natural modes are significantly closer with respect to the clean configuration there is no flutter by coalescence, as the two frequency peaks corresponding to the first two natural modes can be easily distinguished. It can be concluded that the same scenario holds for the experiment; While it is true that noise level preclude from a clear distinction between first two modes, computed and measured power levels are close to the computed values. If flutter by coalescence occurred in the experiment, the magnitude of the peak would have been larger than in the simulation. Again we will consider the peaks between 350 Hz and 400 Hz a consequence of the test section vibratory response. Peak 4 does not appear in the simulation, but peak 5 is well defined. The most important aspect of this is that the frequencies corresponding to peak 4 and 5 are the same for both the configurations (Fig. 20(a) and Fig. 23(a)). The question is if these peaks are caused by the flow-field or are the result of the vibratory response of wind-tunnel components.

The power peak distribution is shown in Fig. 23 for the peak 1/2. Referring to the computed natural modes in

DISTRIBUTION A: Distribution approved for public release.

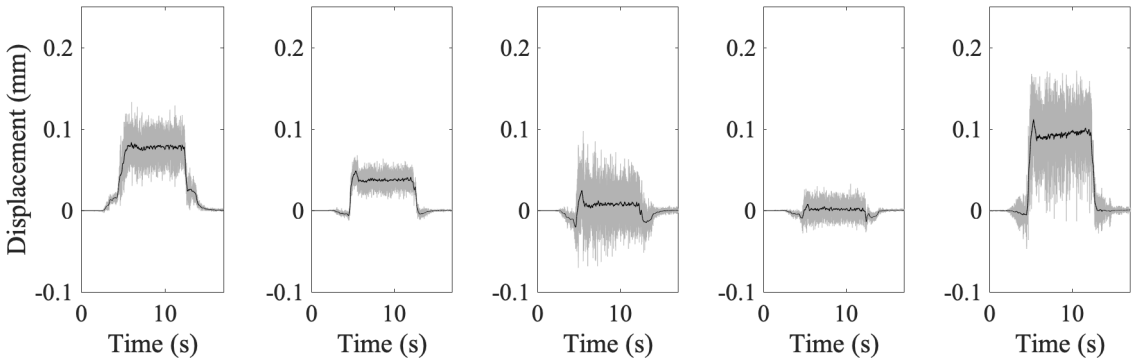

(a) LS2 (0.65L, 0.5W) **(b) LS3 (0.35L, 0.5W)** **(c) LS4 (0.5L, 0.7W)** **(d) LS5 (0.5L, 0.3W)** **(e) LS9 (0.8L, 0.7W)**

Fig. 21 Configuration with pin: Laser sensors (LS) measurements at a sampling rate of 4kHz with an accuracy of 10 μm. the black line represents a mean trend. (Length L = 330 mm, Width W = 230 mm)

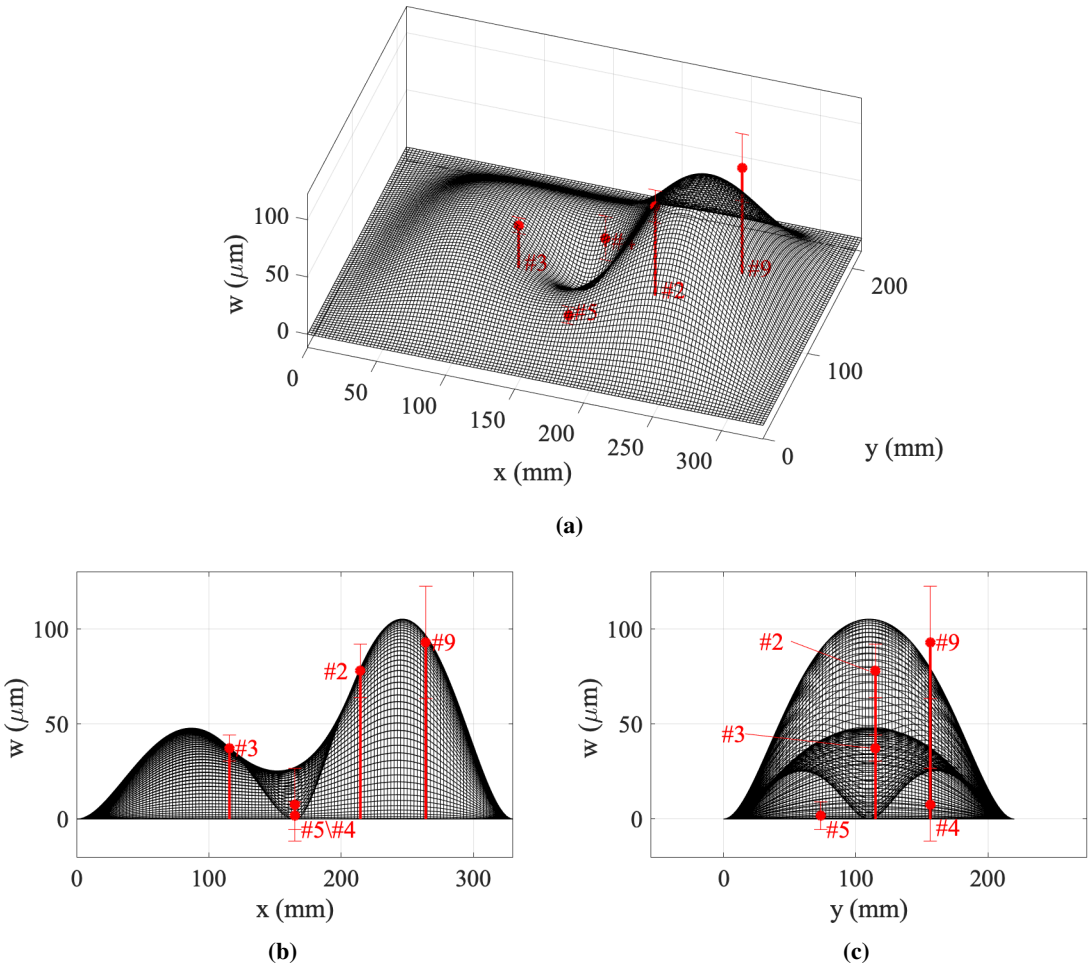

Fig. 22 Configuration with pin: Mean and standard deviation of the displacement measured from the laser sensors (in red) with their respective locations, and computed mean displacement distribution.

DISTRIBUTION A: Distribution approved for public release.

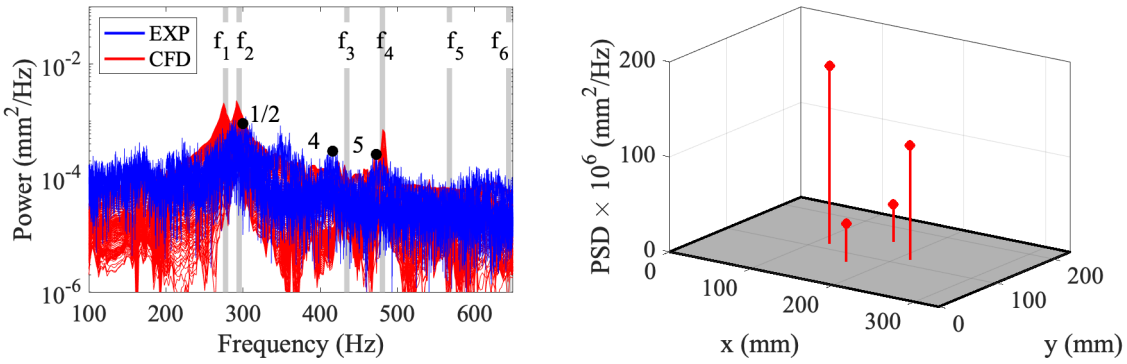

(a) **(b) Mode (exp.)**

Fig. 23 Configuration with pin: (a) Power spectrum density from both laser sensor and simulations at the same query locations and (b) first power peak distribution.

Fig. 13(d), the presence of the first two modes is easily recognizable from the symmetry of the distribution in the spanwise direction and the fact that the peak near the leading edge is larger than the peak near the trailing edge. This last phenomenon is a consequence of the fact that the first mode is asymmetric in the flow direction while the second mode is symmetric, and that the energy content of the two modes is similar.

C. Spectral proper orthogonal decomposition

From the analysis and interpretation of the experiment so far, it is clear that the unanswered question is whether flutter occurs or not, and what is its physical mechanism. The relatively high level of noise in the experiment precludes from a clear identification of the flutter mode that, if present, is likely happening at a higher frequencies than the first two modes. This last observation stems from the fact that modal coalescence is absent and the energy content of first and second oscillation frequency is similar. A spectral proper orthogonal decomposition (SPOD) of the numerical results is conducted for both pressure distribution (on the wind side) as well as panel displacement, in order to clarify the degree and mechanism of fluid-structure coupling. The laser sampling location are mainly located along the panel symmetry lines, which is - as it will be shown - also the locus of modal nodes at higher frequency, *i.e.* those points that theoretically have zero displacement. This negatively impacts the SNR of Fourier analysis. SPOD is instead based on the global modal response of the panel, thus it has a larger SNR. However, it cannot be applied to few discrete laser measurements.

Figure 24 shows SPOD applied to pressure and displacement distribution for both configurations. In Fig .24 (a), a number of peaks are present, with peak 1, 2, 4 and 7 coinciding with the natural frequencies. The dominant peaks 3 and 5, however, are not associated with the natural vibratory response of the panel, thus they appear to be part of the flow characteristic. Figure 24(b) shows the SPOD of the displacement distribution, where the

DISTRIBUTION A: Distribution approved for public release.

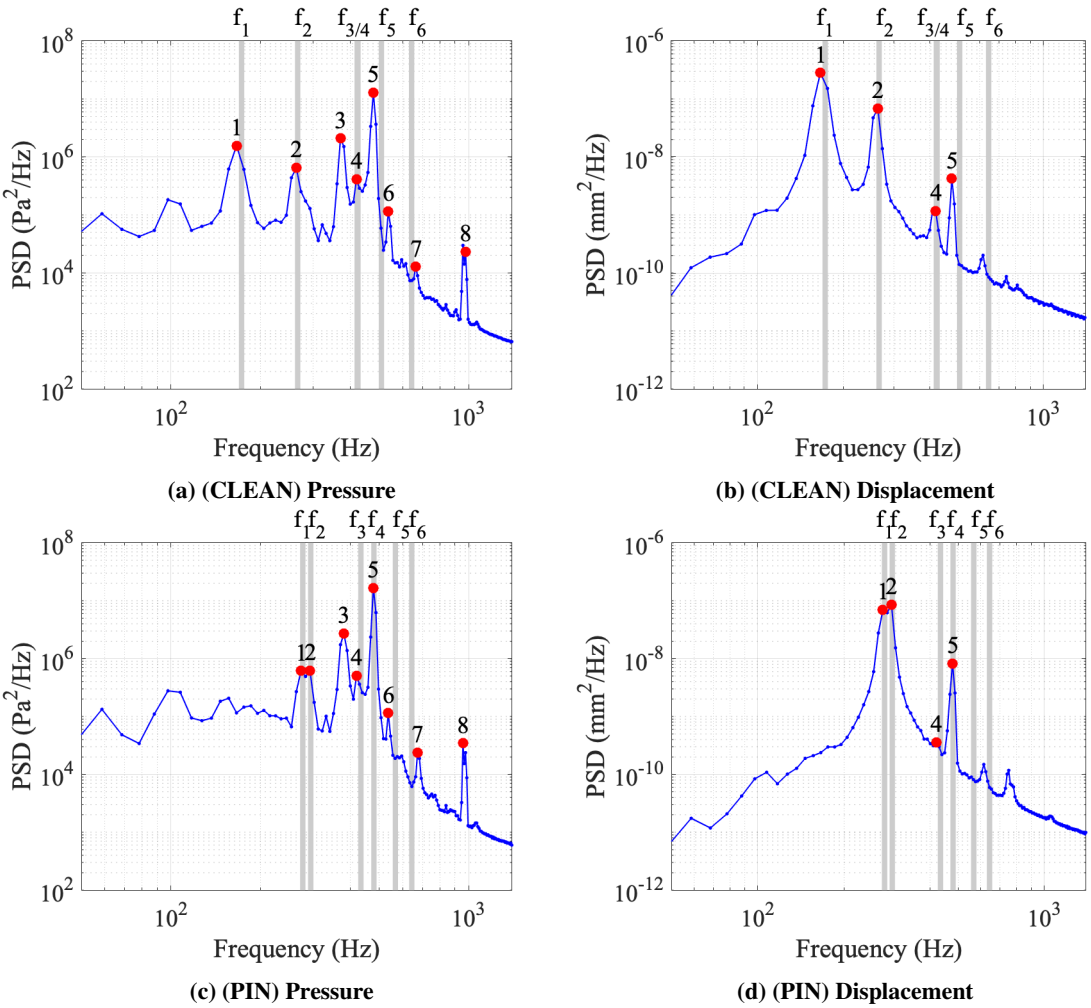

Fig. 24 Power spectrum density computed through a spectral proper orthogonal decomposition of variation in pressure and displacement distribution on the wind side of the panel. Straight vertical line represent the natural frequencies.

red dots represent the peaks corresponding to those in Fig. 24(a). The first three natural modes (peak 1, 2, 4) are excited. Peak 5, the largest SPOD pressure peak, is also visible. By comparison, the power level of peak 5, which is close to the fifth natural mode, is larger than peak 4, which coincides with the third/fourth natural mode. This suggest that the structure peak 5 is mainly caused by a 1-way forced response to an external oscillatory fluidynamic source. If peak 5 was a consequence of 2-way coupling, then its magnitude should have been smaller than peak 4.

Figure 24 (c-d) concern the geometry with a central support. The pressure SPOD in Fig. 24(c) presents again the same dominant peaks 3 and 5 at exactly the same frequencies of the clean geometry, reinforcing the speculation that these actually are flow characteristics, such as induced by shock oscillations. In Fig. 24(c), the peak 5 is very large, being only one order of magnitude smaller than the first two modes. The cause of this is that the peak 5 happens to

DISTRIBUTION A: Distribution approved for public release.

be located exactly at $f = f_4$, thus it is directly exciting this mode. Further investigation is needed to determine why these additional peaks were not so clearly captured in previous frequency analysis carried out in Fig. 20(a) and Fig. 23(a).

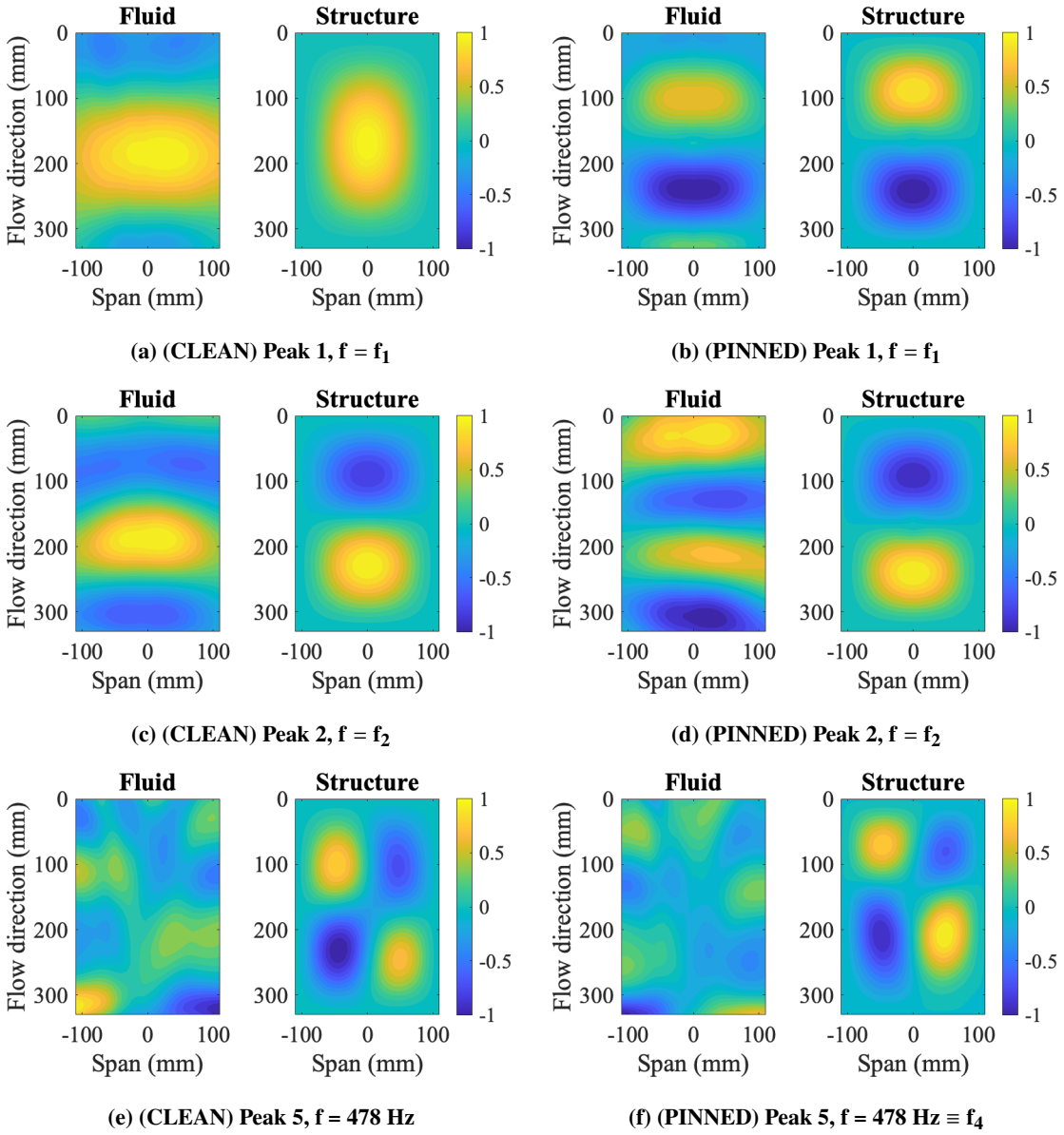

(a) (CLEAN) Peak 1, f = f_1

(b) (PINNED) Peak 1, f = f_1

(c) (CLEAN) Peak 2, f = f_2

(d) (PINNED) Peak 2, f = f_2

(e) (CLEAN) Peak 5, f = 478 Hz

(f) (PINNED) Peak 5, f = 478 Hz ≡ f_4

Fig. 25 Modal analysis relative to the spectral proper orthogonal decomposition performed in Fig. 24.

The modal decomposition is carried out in Fig. 25 in terms of displacement and pressure distributions. The results from the clean geometry are given on the left column, Fig. (a-c-e), while Fig. (b-d-f) shows the results for the configuration with pin. The distributions herein considered are for the most dominant peaks, namely peak 1, 2 and 5. The first two peaks correspond to the first two natural frequencies, consequently f_1 and f_2 are different for the two configurations. The frequency of 478 Hz corresponding to peak 5 is a flow characteristic and thus is the same for both

DISTRIBUTION A: Distribution approved for public release.

the configurations.

Concerning the clean configuration (Fig. 25)(a), peak 1 corresponds to the first natural frequency as it can be seen in the displacement distribution (structure side). The resulting pressure distribution reflects the first mode of deformation but the peak is shifted downstream at around 65% of the length. Another important feature is that, while the displacement magnitude is the largest around the center, pressure levels contours tends to be orthogonal to the flow directions. Similar conclusions, can be drawn for peak 2 (Fig. 25(c)), with the difference that the pressure distribution presents an additional trough towards the end of the plate. Concerning peak 5 in Fig. 25(e), the pressure distribution is significantly different from the structure distribution. The latter is very similar to the fifth natural mode, which is an asymmetric mode in both length and width. Conversely the pressure distribution appears to be the sum of two distributions. The first is a triangular feature, with the leading edge as a base and and the third vertex located along the midspan region at 80% of the length. This is reminiscent of the three-dimensional effects present in the static pressure distribution previously discussed in Sec. IV (see Fig 14(a) flow side). The second feature reflects the structural mode of deformation in that it presents crests and troughs near the side borders of the plate.

A similar outcome is true for the configuration with a pin in the center. At the frequency corresponding to f_1 (in Fig. 25(b)) structure and pressure distributions are very similar. This is likely due to the fact that displacement magnitude is smaller for the configuration with pin, thus resulting in localized pressure variations similar to the displacement distribution. Similar conclusions can be drawn for the peak 2 (Fig. 25(b)), with however an important difference. The structure distribution does not reflect the second mode (which is a symmetric mode of deformation, as shown in Fig. 13(d)), but it appears to be qualitatively very close to the first mode. The possible reason is that the two natural modes are really close to coalescence, and the SPOD does not have the necessary temporal resolution to fully distinguish the two modes. Probably more data points (thus longer computation time) are necessary to completely answer this question. Concerning the peak 5, both displacement and pressure distributions are qualitatively very similar to the clean configuration case. The main difference is that, $f = 478$ Hz is almost coincident with the fourth natural frequency for the pinned configuration.

VI. Conclusion

This work is a fundamental study of transonic panel flutter. This problem was investigated by applying numerical and experimental techniques to obtain a deeper understanding of fluid and structural modes and the interplay between the two. A parametric numerical study in Mach number and altitude was conducted for a Inconel panel (220 X 330 X 1.25 mm) to understand the benefit of pinning the panel at the center. Generally it is possible to conclude that:

- For Mach number values $M_\infty \leq 5$, it was found that thermal buckling as well as an increase in cruise altitude is

DISTRIBUTION A: Distribution approved for public release.

beneficial in terms of dynamic-stability. However, for $2 \leq M_\infty \leq 5$, thermal buckling is more pronounced at low altitudes. Thus, generally, hypersonic flutter was observed for medium-high altitude, where the destabilizing effect of high Mach numbers prevails over the stabilizing effect of low aerodynamic pressure and low thermal buckling. At Mach five, both the configurations undergo flutter; however, the configuration with pin is dynamically unstable for a larger range of altitudes.

- In the transonic regime, the effect of the central pin does not add any benefit.
- In the supersonic regime, the presence of the central pin is stabilizing, especially at low altitudes

The analysis of transonic panel-flutter experiment and simulations for a copper panel (230 X 330 X 2 mm) reveal that:

- In both the configurations, a fluid-dynamic forcing is present inducing oscillating pressure at specific frequencies with very similar power levels and modal pressure distribution.
- The effect of fluid dynamic forcing can be seen in the power density spectrum of the laser-based measurements as two main peaks. However, a SPOD analysis of the computed displacement and pressure distribution has a larger SNR with respect to the fast-Fourier transform of few point measurements. For this reason, numerical simulations are essential in describing this type of panel flutter experiments, characterized by a maximum displacement smaller than 0.2 mm.
- In both the configurations flutter by coalescence of the first two modes is absent
- Sustained oscillations appear to be a result of both freestream noise, which broadly excites all the natural modes but especially the first two, and fluid-dynamic forcing which affects higher modes. When the fluid-dynamic frequency happens to be close to a natural mode, this is excited in a manner similar to resonance. The latter appears to be a 1-way phenomenon, as the frequency and power level of the fluidynamic forcing is the same for the two configurations, thus does not appear to be influenced by the deformations.

Additional studies should be conducted including the effect of pin movement, as the latter might induce a degree of positive damping. For Mach numbers larger than 4, a beneficial effect could possibly be achieved by inhibiting pressure equalization between outer and inner environments. It is necessary to understand if inducing an increase in pressure differential might be a better design choice with respect to local supports. Finally, further work should be oriented towards assessing panel-flutter behavior at Mach numbers larger than five.

VII. Acknowledgment

This work was funded by the Air Force Office for Scientific Research (AFOSR) under the grant FA2386-21-1-4118. Computational and storage resources were kindly provided by the National Center for High-Performance Computing (NCHC) under the grant MOST 110-2222-E-006-002-MY3 from the Ministry of Science and Technology (MOST) now National Science and Technology Council (NSTC). Special thanks go to the Head of the Aerospace Center in Tainan, Director Chung Kung-Ming, and his students, Mr Huang Yi-Xuan and Dr Su Kao-Chun. Lastly, I am again in debt with

DISTRIBUTION A: Distribution approved for public release.

my best friend Dr. Rounak Manoharan for proof-reading this work, making it significantly more understandable.

References

[1] McNamara, J. J., and Friedmann, P. P., "Aeroelastic and Aerothermoelastic Analysis in Hypersonic Flow: Past, Present, and Future," *AIAA Journal*, Vol. 49(6), 2011, pp. 1089–1122.

[2] T.J. Bogar, L. C. J. H., E.A. Eiswirth, and McClinton, C., "Conceptual design of a Mach 10, global reach reconnaissance aircraft," *AIAA 32nd Joint Propulsion Conference and Exhibit*, , No. 96-2894, 1996, pp. 1–10. doi:https://doi.org/10.2514/6.1996-2894.

[3] Varvill, R., and Bond, A., "Application of Carbon Fibre Truss Technology to the Fuselage Structure of the SKYLON Spaceplane," *Journal of the British Interplanetary Society*, Vol. 57, No. 5/6, 2004, pp. 173–185.

[4] F.A. Moslehy, R. D., S.A. Mueller, "Application of laser- based methods and finite element analysis to bond verfication of space shuttle tiles," *Proc. SPIE 2066, Industrial Optical Sensing and Metrology: Applications and Integration*, 1993, pp. 26–35. doi:https://doi: 10.1117/12.162111.

[5] Burns, B., "HOTOL Space Transport for the Twenty-First Century," *Proceedings of the Institution of Mechanical Engineers, Part G: Journal of Aerospace Engineering*, Vol. 204, 1990, pp. 101–110.

[6] Varvill, R., and Bond, A., "The Skylon Spaceplane: Progress to Realisation," *Journal of the British Interplanetary Society*, Vol. 61, No. 10, 2008, pp. 412–418.

[7] Blevins, R., Holehouse, I., and Wents, K., "Thermoacoustic Loads and Fatigue of Hypersonic Vehicle Skin Panels," *AIAA Journal of Aircraft*, Vol. 30, No. 6, 1993.

[8] Dowell, E. H., "Nonlinear aeroelasticity," *A Modern Course in Aeroelasticity*, Springer, 2015, pp. 487–529.

[9] Küchemann, D., "Hypersonic aircraft and their aerodynamic problems," *Progress in Aerospace Sciences*, , No. 2, 1965, pp. 271–353.

[10] Bowcutt, K., "Physics Drivers of Hypersonic Vehicle Design," *22nd AIAA International Space Planes and Hypersonics Systems and Technologies Conference*, 2018, pp. 1–22.

[11] Conners, T., "Predicted Performance of a Thrust-Enhanced SR-71 Aircraft with an External Payload," *International Gas Turbine and Aeroengine Congress and Exposition*, 1995.

[12] Wagner, A., Wartemann, V., Kuhn, M., Dittert, C., and Hannemann, K., "The Potential of Ultrasonically Absorptive TPS Materials for Hypersonic Vehicles," *20th AIAA International Space Planes and Hypersonic Systems and Technologies Conference*, 2015. doi:https://doi.org/10.2514/6.2015-3576.

[13] Shishaeva, A., Vedeneev, V., Aksenov, A., and Sushko, G., "Transonic Panel Flutter in Accelerating or Decelerating Flow Conditions," *AIAA Journal*, Vol. 56, No. 3, 2018, pp. 997–1010. doi:http://arc.aiaa.org | DOI: 10.2514/1.J056217.

DISTRIBUTION A: Distribution approved for public release.

[14] G.A. Davis, O. B., "Transonic Panel Flutter," *34th AIANASMEIASCEIAHSIASC Structures, Structural Dynamics and Materials Conference*, , No. 93-1476, 1993.

[15] Gong, L., Ko, W., and Quinn, R., "Thermal Response of Space Shuttle Wing During Heating Reentry," *NASA Technical Memorandum 85907*, 1984.

[16] Johnson, C. L., *Kelly: more than my share of it all*, Smithsonian Institution, 2012.

[17] Neely, A., Currao, G., and McQuellin, L., "Using Radiative Heating to Perform Fluid-Thermal-Structural Interaction Experiments in a Short-Duration Hypersonic Wind Tunnel," *Proceedings of the 21st Australasian Fluid Mechanics Conference*, 2018.

[18] Tuten, Z., Neely, A., Capra, B., Talluru, K., and McQuellin, L., "Design and Bench Testing of a Radiatively Heated Model for Hypersonic Fluid-Thermal-Structural Interaction Experiments," *AIAA AVIATION 2022 Forum*, 2022. doi:https://doi.org/10.2514/6.2022-3796.

[19] Bhatia, M., and Beran, P., "Design of Thermally Stressed Panels Subject to Transonic Flutter Constraints," *Journal of Aircraft*, Vol. 54, No. 6, 2017, pp. 2340–2349.

[20] Edwards, J., "Transonic Oscillations and Wing Flutter Calculated with an Interactive Boundary Layer Coupling Method," *NASA-TM-110484*, 1996.

[21] Borland, C. J., and Rizzetta, D. P., "Nonlinear Transonic Flutter Analysis," *Journal of Aircraft*, Vol. 20, No. 11, 1981, pp. 1606–1615. doi:http://arc.aiaa.org | DOI: 10.2514/3.7993.

[22] Timme, S., Marques, S., and Badcock, K., "Transonic Aeroelastic Stability Analysis Using a Kriging-Based Schur Complement Formulation," *AIAA Journal*, Vol. 49, No. 6, 2011, pp. 1202–1213. doi:https://doi:10.2514/1.J050975.

[23] Bhatia, M., and Beran, P., "Transonic Panel Flutter Predictions Using a Linearized Stability Formulation," *AIAA Journal*, Vol. 55, No. 10, 2017, pp. 3499–3516. doi:https://doi.org/10.2514/1.J055839.

[24] Muhlstein, L., Gaspers, P., and Riddle, D., "An Experimental Study of the Influence of the Turbulent Boundary Layer on Panel Flutter," *NASA TN-D-4486*, 1968.

[25] Alder, M., "Development and Validation of a Fluid–Structure Solver for Transonic Panel Flutter," *AIAA Journal*, Vol. 53, No. 12, 2018, pp. 3509–3521. doi:http://arc.aiaa.org | DOI: 10.2514/1.J054013.

[26] Menter, F., "Two-Equation Eddy-Viscosity Turbulence Models for Engineering Applications," *AIAA Journal*, Vol. 32, No. 8, 1994, pp. 1598–1605. doi:https://arc.aiaa.org/doi/pdf/10.2514/3.12149.

[27] Wilcox, D., "Simulation of Transition with a Two-Equation Turbulence Model," *AIAA Journal*, Vol. 32, No. 2, 1994, pp. 247–255. doi:http://arc.aiaa.org/doi/pdf/10.2514/3.59994.

DISTRIBUTION A: Distribution approved for public release.

[28] Liu, M., and Gorman, D., "Formulation of Rayleigh damping and its extensions," *Computers and structures*, Vol. 57, No. 2, 1995, pp. 277–285.

[29] "Special Metals (UNS N06617/W.Nr. 2.4663a)," https://www.specialmetals.com/documents/technical-bulletins/inconel/inconel-alloy-617.pdf, ???? Accessed: 2023-10-13.

[30] Chung, K., Miau, J., and Yieh, J., "Initial Operation of ASTRC/NCKU Transonic Wind Tunnel," *AIAA 94-2515 25th Plasmadynamics and Lasers Conference*, 1994. doi:https://doi.org/10.2514/6.1994-2515.

DISTRIBUTION A: Distribution approved for public release.